A Coupled SPH-DEM Model for Micro-scale Structural Deformations of Plant Cells during Drying

H. C. P. Karunasena, W. Senadeera, Y. T. Gu* and R. J. Brown

School of Chemistry Physics and Mechanical Engineering,
Faculty of Science and Engineering, Queensland University of Technology,
2-George street, Brisbane, QLD - 4001, Australia.

Abstract

A single plant cell was modelled with smoothed particle hydrodynamics (SPH) and a discrete element method (DEM) to study the basic micromechanics that govern the cellular structural deformations during drying. This two-dimensional particle-based model consists of two components: a cell fluid model and a cell wall model. The cell fluid was approximated to a highly viscous Newtonian fluid and modelled with SPH. The cell wall was treated as a stiff semi-permeable solid membrane with visco-elastic properties and modelled as a neo-Hookian solid material using a DEM. Compared to existing meshfree particle-based plant cell models, we have specifically introduced cell wall-fluid attraction forces and cell wall bending stiffness effects to address the critical shrinkage characteristics of the plant cells during drying. Also, a moisture domain-based novel approach was used to simulate drying mechanisms within the particle scheme. The model performance was found to be mainly influenced by the particle resolution, initial gap between the outermost fluid particles and wall particles and number of particles in the SPH influence domain. A Higher order smoothing kernel was used with adaptive smoothing length to improve the stability and accuracy of the model. Cell deformations at different states of cell dryness were qualitatively and quantitatively compared with microscopic experimental findings on apple cells and a fairly good agreement was observed with some exceptions. The wall-fluid attraction forces and cell wall bending stiffness were found to be significantly improving the model predictions. A detailed sensitivity analysis was also done to further investigate the influence of wall-fluid attraction forces, cell wall bending stiffness, cell wall stiffness and the particle resolution. This novel meshfree based modelling approach is highly applicable for cellular level deformation studies of plant food materials during drying, which characterise large deformations.

Keywords: SPH; Smoothed particle hydrodynamics; Meshfree; Particle-based methods; Micro-scale cell models; Drying

1. Introduction

Drying is used as a key food preservation technique for around 20% of the world's perishable crops [1]. Plant food materials can contain up to 90% of water by weight [2] and due to such higher moisture contents levels, they are highly susceptible to biological spoilage. During drying, water is removed down to lower limits and it helps to significantly reduce biological reactions and is used as a key food preservation technique in most of the food processing industries. Due to such excessive moisture removal from food tissues and cells, significant microstructural deformations occur which are also highly related with bulk level material deformations. Such structural deformation are very important for quality control and process optimization in food Engineering. These cellular and bulk level deformations at dried conditions are mainly driven by moisture content of plant tissue [3-9] and cell turgor pressure [10]. To relate such governing parameters, micro-scale empirical [3, 5] and theoretical models [11] are frequently used in drying studies. Although, numerical modelling is used as a key engineering tool for a wide range of material deformation studies, according to the best of our knowledge, there are hardly any comprehensive numerical models specifically developed for the micro-scale deformations of food materials during drying. If such models can be developed, those will largely benefit to optimize product quality and processes performance in food processing industries.

In literature, to mimic division and reproduction of cells during tissue development, there are existing plant cell models such as the vertex model [12]. To replicate realistic cells as seen from fresh tissues of some plant varieties, this model involves flatter or linear cell walls. However, there is no guarantee whether this model is capable of handling dried cell characteristics such as shrinkage and cell wall wrinkling. This is further evident by refereeing to the two primary models [13, 14] which were used to develop this hybrid model. Even the three-dimensional vertex cell model [15] developed to study tissue response to external forces, seems not to account for drying related shrinkage characteristics since the model fundamentally involves restrictions for cell area and volume reductions during time evolution. Therefore, it seems that the applicability of vertex models to simulate dried cells is quite challenging.

* Corresponding author. Address: School of Chemistry Physics and Mechanical Engineering, Faculty of Science and Engineering, Queensland University of Technology, GPO Box 2434, Brisbane, QLD 4001, Australia.
Tel.:+61-7-31381009 Fax: +61-7-31381469. E-mail: yuantong.gu@qut.edu.au

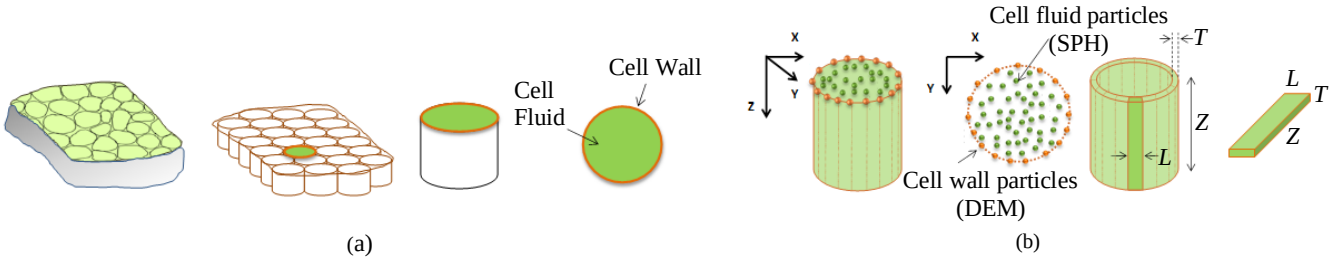

Fig.1. *(a)* 2-D representation of cells in a plant tissue, *(b)* Cell fluid model based on SPH particles and wall model based on DEM particles.

Further, there are several plant cell numerical models reported in the literature that are mainly based on Finite Element Methods (FEM) or Finite Different Methods (FDM), which are primarily developed for basic cell micro-mechanical behaviour studies other than drying [16-20]. These have limited applicability in dried cell modelling because of their fundamental shortcomings in handling complex physics such as: multiphase phenomena due to the presence of liquid, solid and gas phases, excessive cell wall deformations, discrete characteristics of the tissue materials due to the aggregated cellular structure and multiscale relationship between sub-cellular and bulk scale deformations. To overcome such fundamental shortcomings, recently developed meshfree methods seem to be more applicable since they primarily do not use any interconnected grids as in case of FEM and FDM, which entirely rely on grids [21]. In the recent past, much effort has been directed towards the development of different groups of meshfree methods [22] such as the smooth particle hydrodynamics (SPH) [23], the element-free Galerkin (EFG) method [24], and the point interpolation method (PIM) [25, 26], the meshless local Petrov-Galerkin (MLPG) method [27], the local radial point interpolation method [28] and the boundary point interpolation method [29]. These meshfree methods have found many applications in engineering and science [30-32].

Among these methods, smoothed particle hydrodynamics (SPH) is a fairly matured particle-based meshfree technique, which was originally developed for astrophysical applications [23]. SPH defines a given problem domain as a set of non-interconnected particles that carry physical properties which can evolve with time to represent new states of the problem domain in time and space. In our study, the main focus was to characterise extreme deformations of plant cells when their moisture content reduces during drying. For this purpose, we selected SPH specifically because the technique is quite adaptive to incorporate new physics and mechanics into the basic formulations of the method and easily used for most of the hydrodynamic problems of interest [21]. This capability has been proven to work well in plant cell and tissue models where several recent researchers have developed fairly comprehensive plant cell models by coupling SPH with a discrete element method (DEM) to simulate compression, tension, shear of fresh cells [33, 34] and even more critical conditions such as cell breakage and fluid escaping [35]. However, based on the best of our knowledge, there is hardly any SPH based plant cell model specifically developed for cellular deformations during drying.

Accordingly, in this study we hypothesised that a comprehensive numerical model can be developed to investigate different drying mechanisms of cells by adapting the fundamentals of the above mentioned SPH-DEM cell models, along with novel improvements. Further, we hypothesised that the moisture content and turgor pressure can be used as the key controlling parameters for structural deformations at different dryness states. Preliminary results of this work were presented recently [36, 37] and in this paper, we introduce a further refined model, while keeping our scope limited to a two-dimensional (2-D) single cell model. Further, since we involve a fluid dynamic solver in the model (i.e. SPH), other than the basic results presented in this work, the model is even principally applicable for much more dynamic simulations such as in case if dried tissues are subjected to shear or impact loading. Also, by using SPH for the model, we are exploring cellular drying as a new potential application area of meshfree methods, where the outcomes of this approach would contribute to the knowledge front. So, considering all these, we selected the SPH-DEM coupled approach for our cell model.

This paper is organized as follows: firstly the model formulations and assumptions made are presented. Then we introduce how the cell model was used to simulate different cell dryness states along with experimental findings that were used for model validation. Next, several key factors that affect the model performance are discussed. Finally, we present key insights and potential future developments.

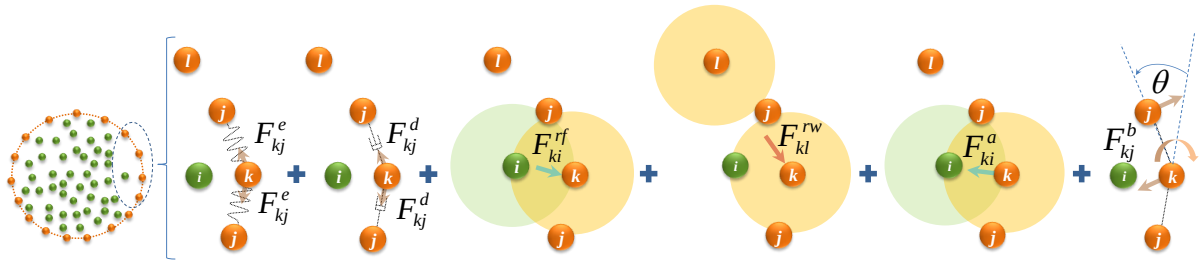

Fig. 2. DEM-based cell wall model uses six types of force interactions: cell wall stiff forces ${F^e}_{kj}$, wall damping forces ${F^d}_{kj}$, wall-fluid repulsion forces ${F^{rf}}_{ki}$, non-bonded wall-wall repulsion forces ${F^{rw}}_{kl}$, wall-fluid attraction forces ${F^a}_{ki}$ and forces due to wall bending stiffness ${F^b}_{kj}$. (i : fluid particles; j, k & l : wall particles)

2. Modelling of a Single Plant Cell

2.1. 2-D representation of a single plant cell

The basic construction of a plant cell was taken as a fluid volume surrounded by a flexible wall such that the cell fluid hydrodynamic pressure is counterbalanced by the tension of the cell wall [9, 17, 19, 20, 38-44]. Considering the aggregation geometry of a simplified tissue as seen in Fig. 1(a), the basic shape of a plant cell was approximated to a cylinder that has a uniform longitudinal cross section. Then, the top circular surface was used as a 2-D model that represents the whole cell assuming uniform axial deformations, neglecting Z directional velocity components and XY plane stresses in top and bottom surfaces [34]. Even thought this is a simplified 2-D representation of an actual 3-dimensional (3-D) cell, still it accounts for cell volume changes and other key cellular mechanisms related with actual cell deformations during drying (see further). The 2-D model has two basic components; a cell fluid which is modelled with SPH and a cell wall which is modelled with a DEM. Accordingly, the cell can be represented using two sets of particles as shown in Fig. 1(b).

2.2. Cell wall model

For the cell wall model, we adapted and further developed a model introduced by several recent researchers [34] which uses a neo-Hookean solid material approximation to account for the visco-elastic characteristics of the cell wall. The model fundamentally uses a set of interconnected discrete elements to represent the cell wall as seen in Fig. 1(b). This element network is modelled using a set of interacting particles which bear properties of each corresponding wall element and wall deformations are referred to as particle displacement characteristics. As seen in Fig. 2, the wall model uses six types of force interactions; cell wall stiff forces (F^e), wall damping forces (F^d), wall-fluid repulsion forces (F^{rf}), non-bonded wall-wall repulsion forces (F^{rw}), wall-fluid attraction forces (F^a) and forces due to bending stiffness of the wall (F^b). F^a and F^b are our new additions to the wall model in order to account for drying related deformations (see further). Thus, the total force (F_k) on any wall particle k was derived using the above set of force interactions as:

$$F_k = {F^e}_{kj} + {F^d}_{kj} + {F^{rf}}_{ki} + {F^{rw}}_{kl} + {F^a}_{ki} + {F^b}_{kj}\,, \tag{1}$$

where for each wall particle k, i are neighbouring fluid particles, j are bonded wall particles and l are non-bonded wall particles. F^e forces were simply defined using a spring model to represent the cell wall resistance to any extensions or contractions. Accordingly, the stiff forces ${F^e}_{kj}$ on any wall particle k due to any bonded wall particle j were calculated individually for each wall element as:

$${F^e}_{kj} = GZ_0T_0\left(\lambda_\theta - \frac{1}{\alpha^2\lambda_\theta^5}\right), \tag{2}$$

where, G is the shear modulus ($\approx E/3$), E is the Young's modulus of the wall material, Z_0 is the initial cell height, T_0 is the initial cell wall thickness, $\lambda_\theta = L/L_0$ is the extension ratio of any cell wall element at the current time step, L is the length of the wall element (distance between particle k and j) at the current time step and L_0 is its initial un-deformed length. Further, the parameter α was calculated with β =0.5 for cylindrical cells as follows [34]:

$$\alpha = \sqrt{\frac{\beta + \sqrt{\beta^2 - 4(\beta - 1)/\lambda_\theta^6}}{2}}, \tag{3}$$

In Eq. (1), F^d forces were to account for viscous characteristics of the fibrous cell wall material and were simply defined using a linear dashpot model. Accordingly, viscous forces ${F^d}_{kj}$ acting on any wall particle k due to the neighbouring wall particles j were calculated as [34]:

$${F^d}_{kj} = -\gamma\, v_{kj}\,, \tag{4}$$

where, γ is the wall damping constant and v_{jk} is the velocity of particle k relative to particle j. Next, the F^{rf}, F^{rw} and F^a forces in Eq. (1) were used to define the wall-fluid interactions and boundary conditions. Here, F^{rf} represents the repulsive forces between fluid and wall particles to ensure all the fluid particles are sufficiently repulsed and maintained within the cell wall. This helps to avoid any undesirable fluid particle penetrations through the cell wall which can cause particle scheme instabilities. As shown in Fig. 2, these F^{rf} forces act through the centre of any interacting wall-fluid particle pair of interest, in an equal and opposite manner (only the forces on wall particle k are shown in Fig. 2). Accordingly, repulsion forces ${F^{rf}}_{ki}$ on any wall particle k due to any other fluid particle i were defined as [21, 34]:

$${F^{rf}}_{ki} = f_{ki}^{rf}\, x_{ki}\,, \tag{5}$$

where, f_{ki}^{rf} is the magnitude of the repulsion force and x_{ki} is the position vector of particle k relative to particle i. The f_{ki}^{rf} is defined according to the Lenard-Jones (LJ) force type as [34]:

$$f_{ki}^{rf} = \begin{cases} f_0^{rf}\left[\left(\dfrac{r_0}{r_{ki}}\right)^8 - \left(\dfrac{r_0}{r_{ki}}\right)^4\right]\left(\dfrac{1}{{r_{ki}}^2}\right) & \left(\dfrac{r_0}{r_{ki}}\right) \geq 1 \\ \\ 0 & \left(\dfrac{r_0}{r_{ki}}\right) < 1\,, \end{cases} \tag{6}$$

where, r_0 is the initial gap between the two particles, r_{ki} is the current gap between them and f_0^{rf} is the strength of the LJ contact. Further, in Eq. 1, to avoid unphysical self penetration of the non-bonded wall particles, a similar approach was used to define the repulsion forces ${F^{rw}}_{kl}$ using a LJ contact strength f_0^{rw}.

Next, we introduce wall-fluid attraction forces for the cell wall model to ensure the cell fluid is not unrealistically separated or detached from the cell wall at any state of cell dryness (see Section 5.2 for more details). For this purpose, the attraction forces ${F^a}_{ki}$ on any wall particle k due to any neighbouring fluid particle i were defined similarly as above using a LJ force type with a LJ contact strength of f_0^a. Here, the attraction forces apply only if the relative distance between fluid and wall particles of each particle pair increases compared to the initial relative distance between them. Further, in Eq. 1, we have incorporated a bending stiffness term (${F^b}_{kj}$) which is also a new addition compared to state of the art particle-based plant cell models [34]. This helps to account for bending resistance that plant cell walls characterise in their fibrous microstructures [45]. Accordingly, the ${F^b}_{kj}$ forces used in the model are to apply resistive forces on wall particles in case if the cell wall tends to undergo unrealistic local deformations or warping (see Section 5.2 for more details). Several recent researchers [46-48] have used cell wall bending stiffness effects in their red blood cell models by applying resistive bending moments based on the local changes of the cell wall curvature. Within any particular particle pair, the corresponding bending moment is finally resolved into equal and opposite forces acting on the two wall particles normal to the wall element (sees Fig. 2). We used a similar concept and the corresponding bending force on any wall particle k within the k and j particle pair was simply defined as:

$${F^b}_{kj} = \frac{k_b}{L} tan\left(\frac{\Delta\theta}{2}\right), \tag{7}$$

where, k_b is the wall bending stiffness, L is the length of any given wall element at any given time step, θ is the external angle between adjacent wall elements as shown in Fig. 2 and $\Delta\theta$ is the change of the θ angle compared to the previous time step. Here, in order to account for the realistic cell wall bending stiffness effects which are mainly driven by the changes of the cell

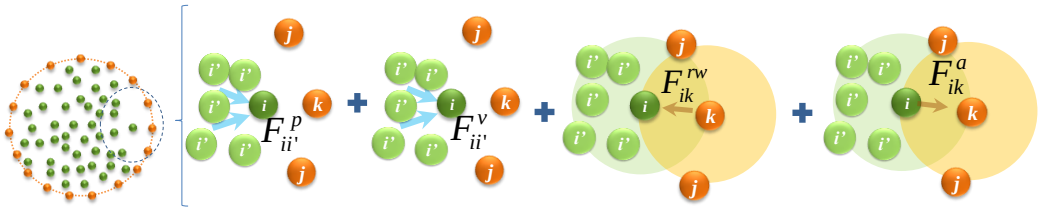

Fig. 3. SPH-based cell fluid model uses four types of force interactions: pressure forces $F^{p}{}_{ii'}$, viscous forces $F^{v}{}_{ii'}$, wall-fluid repulsion forces $F^{rw}{}_{ik}$ and wall-fluid attraction forces $F^{a}{}_{ik}$ (i & i' : fluid particles; j & k: wall particles)

wall curvature, the $tan(\Delta\theta/2)$ function was used other than a simple linear relationship of $\Delta\theta$ since such curvature changes can be better represented by using $tan(\Delta\theta/2)$ than using a linear relationship of θ.

2.3. Cell fluid model

The plant cell interior is mainly occupied by the vacuole and the cytoplasm which contain heterogeneous water-based solutions [9]. With this assumption, researchers [33, 34, 49] have used SPH to model the cell fluid by treating the medium as a Newtonian fluid with low Reynolds number flow characteristics. Here, we used a similar approach and the cell fluid physical properties were approximated to water while the viscosity was set at a higher value to represent realistic viscous cell protoplasm. Accordingly, as seen in Fig. 3, the cell fluid was modelled with four types of force interactions: cell fluid pressure forces (F^{p}), viscous forces (F^{v}), wall-fluid repulsion forces (F^{rw}) and wall-fluid attraction forces (F^{a}). The cumulative effect of these forces was used to define the total force F_i on any fluid particle i as:

$$F_i = F^{p}{}_{ii'} + F^{v}{}_{ii'} + F^{rw}{}_{ik} + F^{a}{}_{ik}\,. \tag{8}$$

According to the standard Lagrangian type SPH equations used to model weakly compressible low Reynold's number fluid flows [34, 50], the momentum equation estimates the pressure forces ($F^{p}{}_{ii'}$) and viscous forces ($F^{v}{}_{ii'}$) for any given fluid particle i as a summed influence from its neighbouring fluid particles i'. These are defined as:

$$F^{p}{}_{ii'} = -m_i \sum_{i'} m_{i'} \left(\frac{P_i}{\rho_i^2} + \frac{P_{i'}}{\rho_{i'}^2}\right)\left(\frac{1}{Z}\right)\nabla_i W_{ii'}, \tag{9}$$

$$F^{v}{}_{ii'} = m_i \sum_{i'} \frac{m_{i'}(\mu_i + \mu_{i'})v_{ii'}}{\rho_i \rho_{i'}}\left(\frac{1}{Z}\right)\left(\frac{1}{r_{ii'}}\frac{\partial W_{ii'}}{\partial r_{ii'}}\right), \tag{10}$$

where at any given time step, m, P, ρ, μ, Z and W are fluid particle mass, cell turgor pressure, density, dynamic viscosity, cell height and the smoothing kernel. For the smoothing kernel W, a more stable quartic smoothing kernel [51] was used in this work other than the frequently used cubic spline which produced significant instabilities in our simulations. The magnitude of the quartic kernel for any given fluid particle i is evaluated as:

$$W_{ij} = \frac{15}{7\pi h^2}\begin{cases} \left(\frac{2}{3} - \frac{9}{8}S^2 + \frac{19}{24}S^3 - \frac{5}{32}S^4\right) & 0 \le S \le 2 \\ \\ 0 & S > 2\,, \end{cases} \tag{11}$$

where, h is the smoothing length at the current time step, S is the ratio of $r_{ii'}/h$ and $r_{ii'}$ is the distance between particle i and any surrounding fluid particle i' within the influence domain of the particle i ($0 \le S \le 2$). From Eq. (5), Eq. (6) and Eq. (7), it can be understood that the smoothing kernel W_{ij} and the value of S play an important role in defining the $F^{p}{}_{ii'}$ and $F^{v}{}_{ii'}$ forces on any fluid particle i as a smoothed and summed influence from the properties of itself and its neighbouring fluid particles i' [51]. We should highlight here that, since the cell dimensions can vary during simulations (see Section 3), the smoothing length h has to dynamically adopt so that the desired average number of particles are always maintained within the influence domain of each fluid particle. For this purpose, a simple geometric relationship was used:

$$h = \left(\frac{D}{D_0}\right) h_0 \,, \tag{12}$$

where, D is the average cell ferret diameter at the current time step, D_0 is the initial cell diameter and h_0 is the initial smoothing length (see Section 2.4). As the system evolves with time, to relate the density and pressure of each fluid particle, the following equation of state was used [21, 34]:

$$P_i = P_T + K\left[\left(\frac{\rho_i}{\rho_0}\right)^7 - 1\right], \tag{13}$$

where, P_T is the initial cell turgor pressure, K is the fluid compression modulus, ρ_i is the density of each fluid particle at the current time step and ρ_0 is the initial density of the cell fluid. Here, the K is an important parameter to ensure the fluid behaves in a sufficiently incompressible manner within the SPH scheme by maintaining the density almost unchanged. It is achieved by setting the K to a higher order value [34]. To update the density of any fluid particle i, the following equation was used [34]:

$$\frac{d\rho_i}{dt} = \frac{1}{Z}\frac{d\rho_i^*}{dt} - \frac{\rho_i^*}{Z^2}\frac{dZ}{dt} + \frac{\rho_i}{m_i}\frac{dm_i}{dt}\,, \tag{14}$$

where ρ_i^* is the 2-D density of particle i defined as $\rho_i^* = Z\rho_i$.

The first term in Eq. (14) accounts for slight density changes of the cell fluid whenever the cell deforms in XY plane and it is defined using the standard SPH continuity density equation as [34]:

$$\frac{d\rho_i^*}{dt} = m_i \sum_{i'} v_{ii'} \cdot \nabla_{\mathrm{i}} W_{ii'}\,. \tag{15}$$

The second term in Eq. (14) adds a correction to the density evolution by compensating for the cell height change and it is defined as [34]:

$$\frac{dZ}{dt} = \frac{Z_t - Z_{t+\Delta t}}{\Delta t}\,, \tag{16}$$

where, at a given time, Z_t, $Z_{t+\Delta t}$ are the cell heights at the previous, current time step respectively and Δt is the time step value. The third term in Eq. (14) accounts for the density changes caused by the change of the fluid particle mass as a result of the moisture transfer through the cell wall due to its permeability. Such mass transfers are mainly driven by the difference between the cell fluid osmotic potential and the turgor pressure. This was accounted in the fluid model by altering the mass of the fluid particles as [34, 38]:

$$\frac{dm_i}{dt} = -\frac{A_c L_p \rho_i}{n_f}(P_i + \Pi)\,. \tag{17}$$

where A_c, L_p, n_f and Π represent total surface area of the cylindrical cell at any given time, cell wall permeability assumed to be isotropic over the cell surface, total number of fluid particles used to model the cell fluid and the osmotic potential of the cell fluid at a given condition, respectively. The latter is carefully set to control the cell turgor pressure [9] because $\Pi \leq 0$ and $P_i \geq 0$ and Eq (13) ensures fluid transfer in to the cell or out of the cell through the cell wall based on the difference between the Π and P_i. This equation is particularly very important in this drying study since the cell deformations are largely governed by the turgor pressure (see Section 3 for more details).

The final two terms in Eq. (8) represent the repulsion forces ${F^{rw}}_{ik}$ and attraction forces ${F^{a}}_{ik}$ act on a given fluid particle i due to the influence of the surrounding wall particles k. These were defined as described in Section 2.2 using a similar LJ force type as:

$${F^{rw}}_{ik} = \sum_k f_{ik}^{rw} x_{\mathrm{ik}}\,, \tag{18}$$

$${F^{a}}_{ik} = \sum_k f_{ik}^{a} x_{\mathrm{ik}}. \tag{19}$$

Table 1. Key parameter values used to model a fresh apple cell

Parameter	Value	Source
Initial cell diameter (D_0)	150 μm	[6]
Initial cell height (Z_0)	100 μm	[34]
Wall initial thickness (T_0)	6 μm	[18]
Initial cell fluid mass	1.77×10^{-9} kg	calculated (see Section 2.4)
Wall mass (= 10% of cell fluid mass)	1.77×10^{-10} kg	calculated [34]
Fluid viscosity (μ)	0.1 Pa s	[33, 34]
Initial fluid density (ρ_0)	1000 $\mathrm{kgm^{-3}}$	set (see Section 2.4)
Turgor pressure (P_T)	200 kPa	[17, 34]
Osmotic potential (Π)	-200 kPa	($\Pi = -P_T$) [34, 49]
Fluid compression modulus (K)	20 MPa	[34]
Initial smoothing length (h_0)	1.3 × initial fluid grid spacing	set (see Section 2.4)
LJ contact strength for Wall-fluid repulsions (f_0^{rf})	1×10^{-12} $\mathrm{Nm^{-1}}$	set (see Section 2.4)
LJ contact strength for Wall-fluid attractions (f_0^{a})	2×10^{-12} $\mathrm{Nm^{-1}}$	set (see Section 2.4)
LJ contact strength for non-bonded wall-wall repulsions (f_0^{rw})	1×10^{-12} $\mathrm{Nm^{-1}}$	set (see Section 2.4)
Wall permeability (L_P)	2.5×10^{-6} $\mathrm{m^2N^{-1}s}$	set (see Section 2.4)
Wall shear modulus (G)	18 MPa	[18]
Wall bending stiffness (k_b)	1×10^{-11} $\mathrm{Nm\ rad^{-1}}$	set (see Section 2.4)
Wall damping ratio (γ)	5×10^{-6} $\mathrm{Nm^{-1}s}$	[33]
Time step (Δt)	1×10^{-9} s	set (see Section 2.4)

2.4. Computational implementation

The above mentioned model formulations were numerically setup with the physical properties of apple cells as given in Table 1. Here, the apple fruit was selected based on the frequent availability of experimental data on physical properties and cellular geometrical changes during drying. In the cell model, the fluid particles were placed on a square grid (without any interconnections) and the same particle gap was used as the initial inter-particle spacing between adjacent wall particles when locating them in the circular boundary around the fluid particles. To calculate the initial cell fluid mass, the initial cylindrical cell fluid volume and the density were used. Here, the initial cell fluid density was assumed to be equal to the density of water. As the model evolves with time, according to Eq. (17), based on the difference between the magnitude of the initially set osmotic potential and the cell turgor pressure, the mass of cell fluid particles tends to change and it lead to slight density variations as defined by Eq. (14) and Eq. (15). Such changes of density cause significant changes of the turgor pressure as given by Eq. (13). These changes of the turgor pressure tend to push the cell wall inwards or outwards, causing cell volume changes. Based on such cell volume changes, the turgor pressure again varies since it needs to be counter balanced by the cell wall tension. These changes of cell turgor pressure will result in cell fluid mass gains or losses according to Eq. (17) and these set the initial conditions for the next round of computations.

During the cell simulations, this computation sequence repeats until the magnitude of the turgor pressure almost equal to the magnitude of the initially set osmotic potential and thereby ceasing any further moisture exchanges through the wall. Then, the summation of the final masses of all the fluid particles is referred to as the steady state total cell fluid mass corresponding to the particular state of cell dryness. Further, it can be seen from Eq. (17), that the time taken to reach steady state conditions can be reduced by increasing the fluid transfer through cell wall by artificially setting the wall permeability to a higher magnitude [34], which would reduce computational cost significantly. Therefore, we used a higher cell permeability as given in Table 1 than a realistic values such as 1×10^{-12} $\mathrm{m^2N^{-1}s}$ [52]. It should be noted here that, if the permeability is set too high compared to the value given in Table 1, the model becomes unstable during time evolution. Also, in this evolution process, a higher K value was used in Eq. (13), so that the fluid density changes are minimized to satisfy the weakly compressible characteristics of the cell fluid within the SPH scheme. The k_b, f_0^a and γ values were selected by following several test simulations to achieve comparable cellular deformations with experimental observations (see further). Similarly, the LJ contact strengths: f_0^{rf} and f_0^{rw} were selected so that that the wall and fluid particles are sufficiently repulsed or attracted and maintained within the cell wall while the cell wall itself is not unphysically displaced. Initial smoothing length (h_0) corresponding to a fresh cell was set as given in Table 1, so that the initial average number of fluid particles in the influence domain satisfies the optimal model performance conditions given in Section 5.1. Further, it should be emphasized here that the cell fluid mass changes in all of the above simulations were achieved by maintaining the same initial number of cell fluid particles while allowing their mass

values to equally change in each time step during the model evolution. Though it seems that this approach doesn't directly replicate the conventional fluid particle diffusion phenomena through the cell wall, as far as our interest is on the deformations achieved at the final steady cell states, the proposed method eventually produces the same final outcome. This method is more advantageous since the cell model and SPH computations become less complex and much more stable than in the case if the particles are allowed to cross the wall boundary. Also a constant number of cell wall particles was used every time and their mass was simply kept constant to represent the dominant solid phase of the cell wall.

To have this model in a computer program, the above mathematical formulations were programmed in C++, and simulations were performed on a multi-core computer with 12 cores on a single Xeon E5-2670 node where each core was a 2.66 GHz processor with 256 GB RAM. The C++ source code was developed by incorporating parallel programming methods and partly adopting an existing SPH source code written in FORTRAN [51]. A Leapfrog integrator [51] was used for the time integration with a sufficiently small time step (see Table 1) to satisfy the minimum time step limits defined by the Courant-Friedrichs-Lewy (CFL) stability criterion [51]. To avoid any undesirable fluid particle penetrations through the wall boundary, in addition to the above mentioned cell wall particles, a same number of massless virtual particles were used to further repulse the fluid particles and were located at midpoints of all wall elements [34, 51]. The Open Visualization Tool (OVITO) [53] was used for the visualizations of the particle model.

3. Modelling of Cell Dryness States

In real drying processes, steady state cellular deformations are attained after a lengthy drying cycle that usually last for many hours in real time. Since a very small time step is used for the model computations (see Section 2.4 and Table 1), if a time domain-based simulation approach is used, it is almost impossible to simulate such lengthy processes completely, because of the excessive computational cost. Based on the background details presented in Section 1 and Section 2.4, since the moisture content and turgor pressure are the key driving parameters for the cellular deformations, we employed a moisture-domain based simulation approach in our work instead of a direct time-based approach. Therefore, different cell states that correspond to distinct moisture contents and cell turgor pressures were simulated as a set of independent simulations. In each case, the cell model was initiated accordingly (see further) and was allowed to settle at the desired cell moisture content and the turgor pressure, while undergoing corresponding deformations until the cell reaches steady state condition.

Here, based on the cell turgor pressure, two stages of cellular deformations were hypothesized and two different criteria were used to attain distinct moisture contents in each case. Firstly, if a general drying process of a plant cell is considered, in its initial stages, the cell turgor pressure tends to reduce gradually with the moisture content reduction [10], and it was hypothesized that this stage exists until the turgor pressure reaches the atmospheric pressure (0 kPa). Therefore, drying simulations for this stage were conducted with osmotic potentials that ranged from the fully turgid condition -200 kPa (as given in Table 1) to 0 kPa, which represents the most critical state of cell dryness within this initial stage. For example, if a partly dried cell which has a 100 kPa turgor pressure is to be simulated, the targeted final turgor pressure becomes 100 kPa. So, to achieve this, according to Eq. (17), the osmotic potential needs to be set to -100 kPa and the turgor pressure is initiated to 100 kPa. Also, the masses of all fluid particles need to be equally initiated so that the total summation of the particle mass becomes equal to the total initial cell fluid mass given in Table 1. Also the cell wall particle mass is kept constant at the value given in Table 1. Now, with the time evolution of the cell, the turgor pressure evolves and reaches 100 kPa and in the meantime, the cell moisture content reduces from $X/X_0 = 1.0$ to slightly lower values such as $X/X_0 = 0.95$ (see Section 5.2 for the complete set of results), which is basically due to the moisture exchange through the cell wall. Further, as the turgor pressure remains positive in any state within this first stage, the cell shape can be expected to remain almost circular since the cell fluid highly tends to push the cell wall outwards. Now, the final cell properties are used to characterise this partly dried cell which has 100 kPa turgor pressure. This approach was used to simulate any of the cell states within the first stage of cellular deformations.

Next, to simulate any of the further dried cell states beyond the above mentioned 0 kPa state, a different approach was used in order to account for the unique turgor pressure characteristics hypothesized. When comparing with the above stage, the moisture content values of this second stage is usually lower and the turgor pressure can be assumed to remain equal to the atmospheric pressure without any further decrements [54]. This can mainly be assumed because of the pressure equilibrium that can exist between the atmosphere and the cell fluid due to the highly flexible and relaxed cell wall in these flaccid cell conditions. Thus, to accommodate for the excessive cell fluid volume reductions, the cell wall can be assumed to deform at a higher degree such that the cell deviates from its initial circular shape. Accordingly, the dried cell simulations of this stage were always conducted with an artificially set osmotic potential of 0 kPa to ensure the cell turgor pressure is maintained at the atmospheric pressure of 0 kPa according to Eq. (17). Then, as the cell evolves with time according to Eq. 17, a limitation arises on the moisture transfer through the cell wall since both the P and Π remain around 0 kPa. Such a limited moisture transfer through the cell wall is usually inadequate to achieve the corresponding lower moisture contents within this stage. Because of

this, the initial cell fluid mass was manually set to the desired value prior to each simulation run within this stage. Thereby with the time evolution, the cell reaches steady moisture content values close to the desired values. For example, to simulate a cell state corresponding to a normalized moisture content of 0.5, masses of all the fluid particles needs to be equally initiated so that the total fluid mass becomes half of the cell fluid mass value given in Table 1. Then during the simulation, the osmotic potential needs to be kept fixed at 0 kPa and the turgor pressure is initiated to 0 kPa. The wall particle mass is kept constant at the value given in Table 1. As the model evolves with time, a steady state condition is attained where the normalized cell moisture content almost equals to 0.5 and the turgor pressure will remain around 0 kPa. Now, the corresponding cellular geometrical parameters (see further) are calculated and used for characterising this state of cell dryness. This method was used to simulate any of the cell states which correspond to the second stage cellular deformations.

After each of the above simulations, the steady state cellular deformations were quantified using several geometrical parameters [3]: cell area (A), ferret diameter[1] (D), perimeter (P), roundness[2] (R), elongation[3] (EL) and compactness[4] (C). These were compared against the dry basis moisture content ($X = kg_{water}/kg_{dry\ solid}$) and to facilitate easy comparison, all of these parameters were converted into normalized parameters (X/X_0, A/A_0, D/D_0, P/P_0, R/R_0, EL/EL_0 and C/C_0) by dividing each by the corresponding initial value (X_0, A_0, D_0, P_0, R_0, EL_0 and C_0) related to the fresh condition. These simulation results were compared with experimental data on apple cellular deformations obtained from our experiments [55] and literature [3]. The results are presented in Section 5.

We should highlight further that, in all above simulations, the cell was considered as a thermodynamic open system that has a flexible boundary (cell wall). Therefore, mass and energy can cross the boundary and at different states we focused only on the deformations of the system and its boundary (cell and cell wall). Also, in each simulation setup, a new system was used that owns a particular initial mass corresponding to its initially set moisture content. In each time step, when the cell evolves with time, small amounts of mass (cell fluid) crosses the boundary until the system reaches steady state condition with no further mass transfers through the boundary (such mass transfers were referred as changes of the cell fluid particle mass, without actual particle movements across the boundary). Theoretically, due to the change of mass within the system (cell), there can be slight temperature variations in the system, but were not considered within the scope of this research, since our preliminary objective was to study only the cell deformations mainly driven by the mass transfer. However, such possible temperature fluctuations can be assumed to be fairly small when considering the relatively small time scales we are referring in these micro-scale simulations.

4. Drying Experiments and Cell Geometry Analysis

To validate the simulation results, we conducted a series of laboratory experiments and obtained apple cellular structural deformation data as a function of normalized moisture content of apple fruit [55]. Here, due to the practical difficulties of conducting single cell based drying experiments along with moisture content and other geometrical parameter measurements, we performed tissue drying and thereby observed cell-wise average deformations. Though these tissue-based results are having influences from intercellular bonds in addition to the individual cell-wise deformation, still these tissue results do provide useful insights on individual cellular deforestations. Therefore, we used these tissue-based results to preliminary validate the single cell model developed in this work.

For this study, Gala apple variety purchased from a local supermarket in Brisbane-Australia was used that had an initial wet basis moisture content ($kg_{water}/kg_{wet\ solid}$) of 0.84 ± 0.01. With the use of manual cutting methods, ring shaped slices of outer diameter 60 mm and inner diameter 25 mm were obtained from the middle parenchyma region of the fruit and pre-treated with a 3% citric acid solution for 1 minute. Using these samples, a series of drying experiments were conducted in a hot air oven dryer that maintains an air velocity of 1.5 ms^{-1} and a temperature of 70 ℃ as the drying environment. For these experiments, independent samples were used and dried individually for 30, 60, 90, 120, 150, 180 and 210 minutes. At the end of each individual drying cycle, the corresponding dried samples were taken out of the dryer and one half of them was used for moisture content measurements while the other half was used for microstructural investigations. The moisture content measurements were done using a digital weighing scale. Initial weights of the oven-dried samples were recorded and then subjected to a secondary drying process at 100 ℃ for about 18 hours to obtain the dry mass of the samples. Using these mass values, dry basis moisture content was calculated for each sample. All the experiments were repeated once and average results were taken for comparison and analysis.

[1] $\sqrt{4A/\pi}$
[2] $4\pi A/P^2$
[3] major axis length/minor axis length
[4] $\sqrt{4A/\pi}$ /(major axis length)

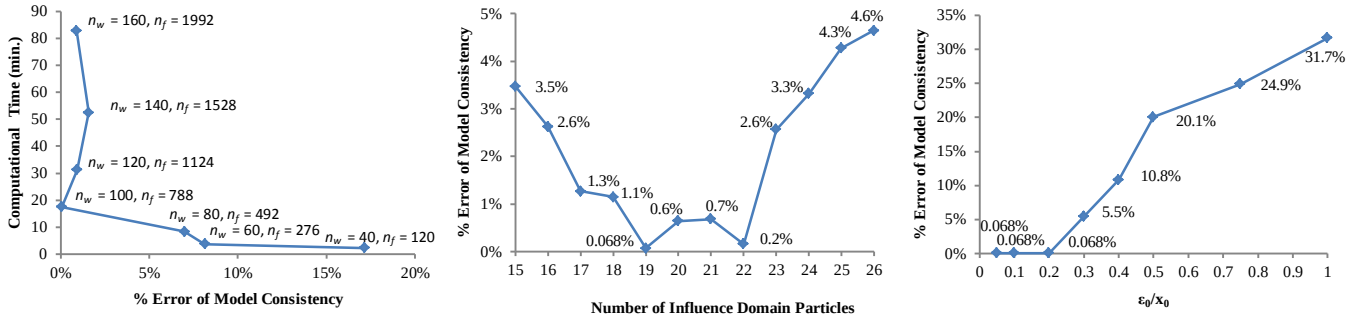

(a) (b) (c)

Fig. 4. *(a)* % error of model consistency and computational time as a function of the particle resolution, % error of model consistency as a function of: *(b)* the average number of particles in the influence domain of each fluid particle, *(c)* ε_0/x_0. (n_w: number of wall particles; n_f: number of fluid particles; ε_0: minimum allowed gap between the outer most fluid particles and the wall particles at the initial particle placement; x_0: initial fluid particle spacing)

To facilitate microstructural examination, representative portions of oven dried samples in each case were used and were cut in to cubic specimens of 10 mm × 5 mm × 5 mm. These were initially coated with a fixative solution containing 2.5% glutaraldehyde, 4% paraformaldehyde, and 0.1 M cacodylate buffer (pH 7.2) and stored at 4℃ for about 12 hours. Then a 0.1 M cacodylate buffer (pH 7.4) was used to rinse the samples before post fixing with cacodylate-buffered 1% osmium tetroxide for 4 hours in room temperature. Next, the samples were dehydrated using ethanol solutions of incremental concentrations of 50%, 70% and 90% twice for 10 minutes in each case. The samples were finally dehydrated once in a 100% ethanol solution for 10 minutes. These dehydrated samples were then dried twice for 30 minutes using a Critical Point Drying [56, 57] apparatus. These prepared samples were fractured by freezing in liquid Nitrogen to obtain freshly cut sections for microscopic examinations. This method of fracturing helps to avoid any undesirable indentations appearing on the tissue surface if any mechanical fracturing methods are involved. One could doubt that freezing of samples in liquid Nitrogen might cause some shrinkage in the structure which would affect the measurements. But, it should be noted here that, it is a standard technique used in SEM imaging to produce freshly cut cross sections and the technique essentially uses fixative solutions on the samples to fix their structure prior to this freezing phase such that the cell structure would hardly get altered during the freezing process. However, even if there are any such minor effects, those will equally influence on all the samples and such effects will get almost cancelled out when normalized cellular parameters are calculated (see Section 5.2).

Then, the samples with such freshly cut cross sections were mounted on metal stubs using double sided carbon tape followed by sputter coating up to 10 µm of gold using an automated sputter coater. Eventually the specimens were examined at 20 kV in a FEI Quanta 200 Environmental Scanning Electron Microscope (SEM). The samples were observed at the centre, along their cross section and imaged at 200× magnification with an image size of 885 × 1022 pixels. These SEM images were finally analyzed by the ImageJ software (version 1.46) and the average cell area, ferret diameter, perimeter, roundness, elongation and compactness were quantified and recorded.

5. Results and Discussion

5.1. Determination of the optimal particle scheme for the cell model

Performance of SPH models are largely influenced by the particle resolution [34, 58], number of particles in the influence domain [21, 58] and the initial relative position of boundary and interior particles [58, 59]. To study such effects in the proposed cell model, a series of numerical studies were conducted on a fully turgid cell. Firstly, the particle resolution was changed and optimum particle resolution was targeted so that the computational efficiency and accuracy of computations are simultaneously optimized. As mentioned in Section 2.4, since the fluid grid spacing and the wall particle gaps are equally set, in a given model setup, the number of fluid particles (n_f) is proportional to the corresponding number of wall particles (n_w) and therefore in these tests, n_w was simply used as a parameter to alter the total number of particles used in the model. Thus, several numerical tests were conducted by setting the n_w to 40, 60, 80, 100, 120, 140 and 160 and the percentage error of model consistency[5] and the computational time in each case were recorded and compared (Fig. 4(a)). In these simulations, the average number of particles in the influence domain was maintained at around 20 to ensure better model accuracy [21]. Here, the percentage error of model consistency was calculated by comparing the model predictions on the average hoop directional

[5] % error of model consistency = 100 × (cell wall tension predicted by the model – theoretical cell wall tension) / theoretical cell wall tension

inter-particle cell wall force and the corresponding theoretical cell wall tension[6] as done by recent researchers in their SPH-DEM cell models [34].

It is evident from Fig. 4(a) that higher particle resolutions generally produce minimum error bounds up to a particular particle number and thereafter the error increases slightly. When referring to error analysis studies of meshfree particle methods [60], this phenomenon has been reported where the consistency error can increase when the smoothing length is reduced while maintaining a constant ratio between the smoothing length and the initial particle spacing. This is true for our higher resolution models since we kept a constant 1.3 ratio between the smoothing length and the initial particle spacing and therefore the actual smoothing length of higher resolution models are smaller. However it should be noted here that the possible error increment is not very significant as can be seen from Fig. 4(a) and we did not further analyze this effect in this work. Next, from Fig. 4(a), it is further seen that the computational time directly increases with the particle resolution. This is mainly due to the higher number of interaction computations in higher resolution models. So, by considering both the accuracy and the computational cost factors within the studied particle number range, we selected 100 wall particles as the optimum particle number for our cell model and the corresponding fluid particle number was 788. This medium resolution model was mainly used for this work and in Section 5.7 we have further elaborated how particle resolution can influence simulation outcomes.

Secondly, using the optimized particle resolution found from the previous study (n_w = 100 and n_f = 788), a set of secondary studies were conducted to determine the optimal number of particles to be maintained within the influence domain of each fluid particle of the SPH fluid model, such that the percentage error of model consistency becomes further reduced. Accordingly, the ratio of the initial smoothing length (h_0) to the initial fluid grid spacing (x_0) was varied to obtain different influence domain particle numbers and here we limited our study to a range of 15 to 26 particles. As seen in Fig. 4(b), the cell model accuracy was optimized if the average number of particles in the influence domain becomes 19 (excluding the base particle) which was achieved by setting the $h_0/x_0 \approx 1.3$. This finding closely agrees with the standard recommendations for 2-D computations in SPH [21].

Finally, using the optimal result parameters obtained from the above two studies, a further set of studies were conducted to improve the model consistency by optimizing the initial relative placement of fluid and wall particles [58]. The relative placement was characterized by the minimum allowed gap (ε_0) between the outer most fluid particles and the wall particles at the initial particle placement. This was achieved by limiting the maximum radius of initial particle placement by keeping a blank gap of ε_0 just before the cell wall. The ε_0 was varied in steps from higher values to lower values and the highest ε_0 used was equal to the initial fluid grid spacing (x_0). As shown in Fig. 4(c), it is clearly seen that, the model consistency is highly sensitive to ε_0/x_0 and by maintaining $\varepsilon_0/x_0 \leq 0.2$, the model consistency error could be minimized. A similar finding of $\varepsilon_0/x_0 \leq 0.3$ has been reported in SPH-based conduction modelling of a disk with isothermal boundary particles [58]. So, eventually by using the overall outcome of these tests, we were able to limit the percentage error of model consistency down to 0.07%, which is a significant achievement compared with the existing SPH-DEM cell models [34] which possess around 4% to 7% consistency errors. Further, as mentioned in Section 2.4, during these simulations, the cell fluid incompressibility was fairly well achieved by limiting the density fluctuations within 0.0005%.

5.2. Cell deformations at different dryness states

Using the optimized model parameters obtained as described in Section 5.1, cellular deformations were simulated at different moisture contents and turgor pressure values, starting from a fresh cell (X/X_0 = 1.0 and P_T = 200 kPa), to a critically dried cell (X/X_0 = 0.2 and P_T = 0 kPa). The snapshots of the particle scheme visualizations are presented in Fig. 5. In Fig. 5(a), the initial particle scheme is shown where the fluid particles are placed in a square grid surrounded by the circular wall boundary. In Fig. 5(b) a snapshot of steady state cell model geometry is presented which was obtained after simulating a fresh cell. When comparing with the initial conditions (Fig. 5(a)), the fresh cell has inflated and increased its dimensions slightly and the circular shape is well maintained. Next, in Fig. 5(c), a partly dried cell at 100 kPa turgor pressure is presented. Since the turgor pressure is positive, this state corresponds to the first stage of cellular deformations as discussed in Section 3 and the cell shape remains circular. Next, from Fig. 5(d) to Fig. 5(g), the second stage of cellular deformations are observed as discussed in Section 3, where the cell gradually experiences higher degree of deformations. It is seen that, as the moisture content reduces, the cell wall warping effects become dominant where many localized bends tend to form and the cell shrinks in order to accommodate the reducing cell fluid volume. When referring to SEM images as seen from Fig. 6, similar cellular deformations are observed for actual cells which undergo cellular shrinkage during drying with increased cell wall warping. Further, the experiments indicate that the fresh cells are not quite circular (see Fig. 6(a)) as we hypothesised in this model. It is mainly due

[6] Theoretical cell wall tension = turgor pressure × cell height × cell radius

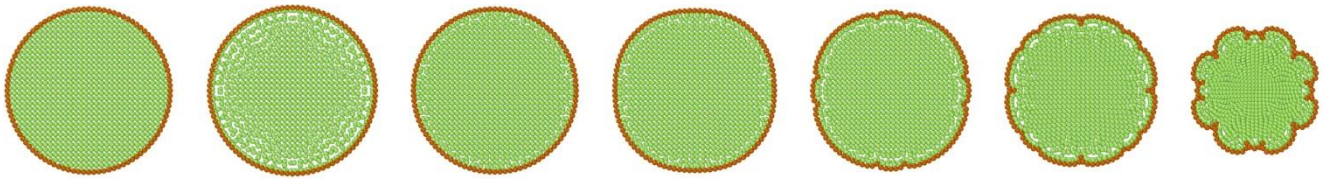

Fig. 5. Snap shots of the cell model visualizations at: (a) initial particle distribution before simulations, (b) turgid condition X/X_0 = 1.0, dried conditions: (c) X/X_0 = 0.95, (d) X/X_0 = 0.8, (e) X/X_0 = 0.6, (f) X/X_0 = 0.4 and, (g) X/X_0 = 0.2.

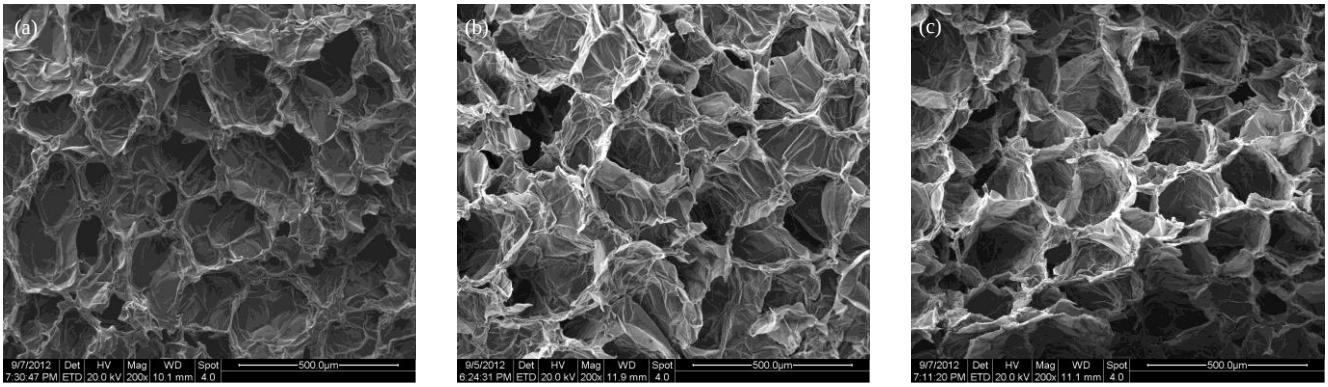

Fig. 6. SEM images of apple cells in different states of dryness: (a) X/X_0 = 1.0, (b) X/X_0 = 0.5, and (c) X/X_0 = 0.2.

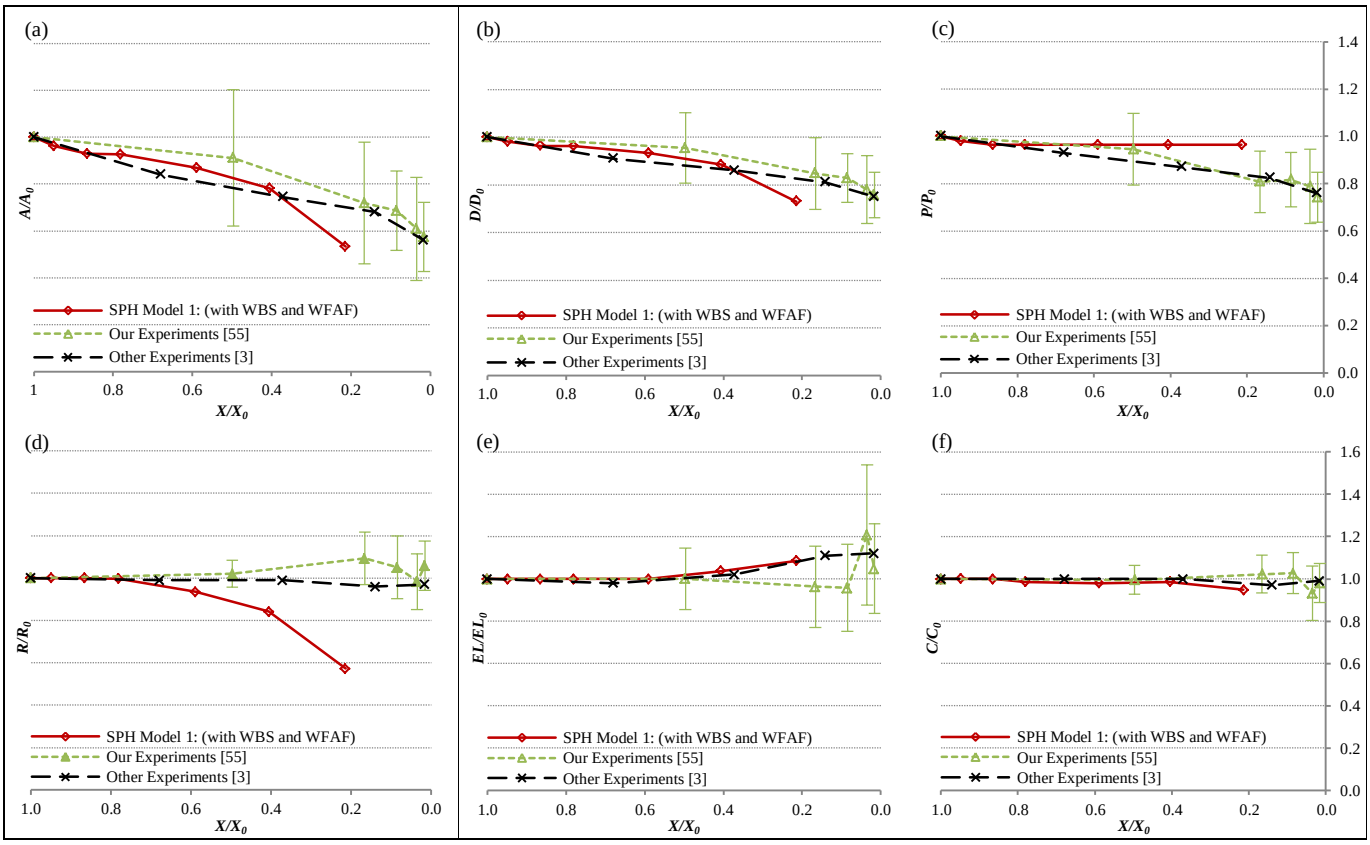

Fig. 7. Cellular geometric parameter variations as a function of the cell moisture content: (a) A/A_0, (b) D/D_0, (c) P/P_0, (d) R/R_0, (e) EL/EL_0, (f) C/C_0. (Error bars indicate one standard deviation)

to the intercellular contacts present in plant tissues. To account for such effects, more advanced tissue models are needed. But, still even for such models, outcome of the current research work will be very useful since this single cell model could be used as a building block to build tissue models by aggregation.

To quantify and compare the cellular geometric parameters in more detail, we further studied different cellular geometrical parameters as described in Section 3 and the results are presented in Fig. 7. When the A/A_0 trend is considered, as seen in Fig. 7(a), up to X/X_0 = 0.4, the A/A_0 reduces in a good agreement with the experimental results and beyond that, decreases steeply. This may be due to the limitation of our single cell model which has no external restrictions for deformations which is not the case for real cells in tissues which have intercellular bonds. Next, in case of D/D_0, a similar trend is observed as seen in Fig. 7(b) and this can be explained similarly as above. When referring to Fig. 7(c), the P/P_0 trend is such that, as far as there is a positive turgor pressure, cell perimeter continues to decrease with the X/X_0 reduction. This trend seems to exist when $0.85 \leq X/X_0 \leq 1.0$ and it corresponds to first stage of cellular deformations as discussed in Section 3. In this stage, since the cell wall usually has a higher tension which is proportional to the turgor pressure, the cell wall total length (cell perimeter) reduces as the turgor pressure drops. Next, when the moisture content is further reduced, the P/P_0 trend demonstrates the second stage of deformations, where in the absence of a sufficient positive turgor pressure, the cell wall basically tends to warp-up or reorient without any significant perimeter contractions. Such a model behaviour is mainly due to the influences of the cell wall force fields, where only the wall-fluid attraction forces would contribute to any such contractions. But since the attraction forces always act normal to each of the wall elements, they mainly result in area or diameter contractions rather than perimeter contractions. However, according to the experimental findings, we can observe that the perimeter continues to decrease with the moisture content. This opens a potentially interesting research question, whether the turgor pressure remains positive throughout the drying cycle when the moisture continues to remove from the cell even at extremely dried conditions. Sometimes this perimeter reducing phenomenon may also be due to the moisture removal from the cell wall and related wall contractions, which were not accounted in our model. These highlight the need for more detailed experimental findings on cell turgor pressure behaviour and moisture dynamics during drying, along with further improved cell wall models, so that the numerical predictions will become more comparable.

Next, in Fig. 7(d), the R/R_0 of the model tends to reduce quite considerably beyond X/X_0 = 0.8, with respect to the real cells. According to the definition of the roundness (see Section 3), this reducing trend is a resultant effect of the slightly diverse trends of cell parameter and cell area which were discussed above. In addition to these reasons, tissue related deformation resistance can also affect to maintain such higher R/R_0 values in real cells. Next, if the EL/EL_0 trends are considered, as seen in Fig. 7(e) the model closely mimics the increasing trend shown by the both experimental curves. Since the elongation is governed by the minor axis and major axis lengths, the model's overall geometrical deformation predictions can be considered as closer to the actual cells. When considering the C/C_0 trend as shown in Fig. 7(f), a qualitatively good agreement is observed when compared with the experimental findings, where the compactness remains mostly unchanged during drying. These trends indicate that even though we used a single cell model, still it has the capability to mimic drying originated deformations of actual cells up to a promising level. These findings provide clues for the appropriateness of this novel method to simulate dried plant cell and the importance of extending the model up to tissue scale while improving the single cell model itself.

5.3. Significance of wall bending stiffness and wall-fluid attraction forces for model performance

The influence of the newly introduced cell wall bending stiffness (WBS) effects and cell wall-fluid attraction forces (WFAF) to the model performance were firstly studied qualitatively by a visual comparison as seen in Fig. 8. When compared with the original cell model which involves both WBS and WFAF (Fig. 8(a)), if the WBS effects are omitted, as seen in Fig. 8(b), the cell significantly loses its basic circularity even at moderately dried conditions. Further, in case of critically dried states such as X/X_0 = 0.2, the cell wall tends to have unrealistic local sharp edges. Next, as seen in Fig. 8(c), if the WFAF effects are omitted, cell fluid unrealistically separates from the cell wall (see X/X_0 = 0.2 in Fig. 8(c)). Further, when Fig. 8(d) is considered, the cell deformations seem to be not quite acceptable when both the WBS and WFAF effects are omitted in the model. These findings clearly imply that the existing SPH based plant cell models are not suitable for drying studies since they do not involve WBS and WFAF, and our proposed modifications are essential. It should be further noted here that, when considering all the fresh cell states in Fig. 8, they are almost identical without much of WBS and WFAF influence. This implies that the WBS and WFAF effects mainly influence the dried cell conditions other than fresh cell conditions that possess highly stretched cell walls and higher turgor pressures to keep the cell fairly unwrapped and well pushed outwards by the cell fluid.

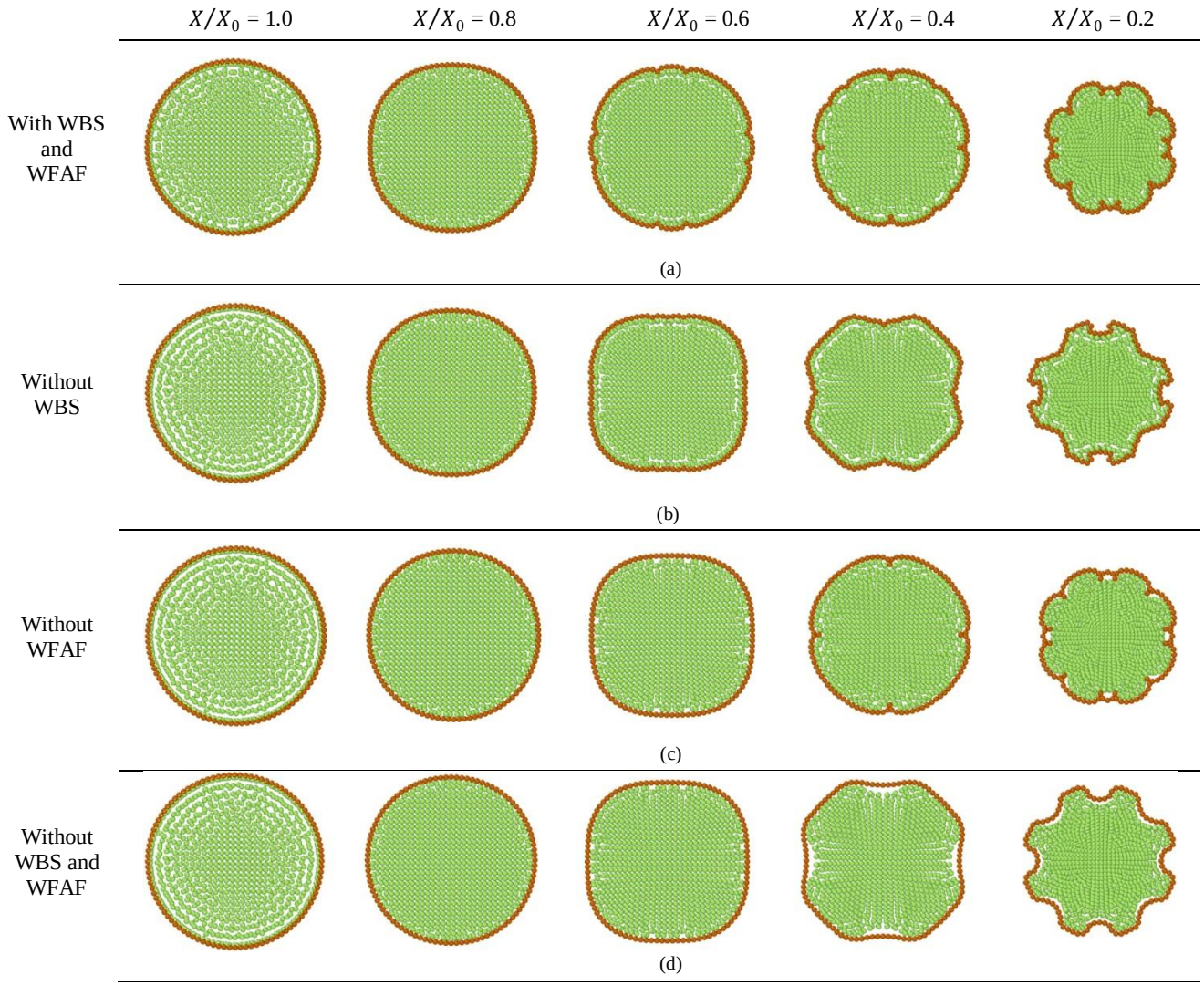

Fig. 8. Effects of cell wall bending stiffness (WBS) and cell wall-fluid attraction forces (WFAF) on cellular deformations: (*a*) with both WBS and WFAF effects. (*b*) without WBS effects. (*c*) without WFAF. (*d*) without both WBS and WFAF effects.

To further elaborate these effects, the usual normalized cellular geometrical parameters were then studied and are presented in Fig. 9. As described in Section 5.2 we should emphasize here that, although there are some limitations of the single cell model when comparing with the tissue based experimental results, still the insights drawn from the single cell based predictions are important for more advanced model development. In this background when considering Fig. 9(a) and Fig. 9(b), it is clearly observed that the model 1 and 2 satisfactorily mimic the gradual decreasing trend of the cell area and ferret diameter, while the model 3 and 4 have not accounted for the shrinkage during the intermediate stages of drying ($0.4 \leq X/X_0 \leq 0.85$). These observations indicate the importance of the WFAF introduced in this work to better mimic the cellular shrinkage during drying. However, from Fig. 9(c), there is hardly any difference observed between the model predictions which may be mainly due to the limitations of the current model which does not account for cell wall contraction effects as described in Section 5.2. Further, during the extremely dried conditions ($0.2 \leq X/X_0 \leq 0.4$), Fig. 9(a) and Fig. 9(b) seem to indicate that the model 2 performs slightly better than the model 1. But, when Fig. 9(e) and Fig. 9(f) are considered, model 2 deviates considerably from the experimental curves at the intermediate stages of drying ($0.3 \leq X/X_0 \leq 0.8$) which is more critical than the opposite trend observed from extremely dried states of Fig. 9(a) and Fig. 9.(b). At the same time, when the cell visualizations are referred as presented in Fig. 8(b), it is clearly observed that in order to avoid unrealistic sharp bends of the cell walls, WBS effects are important. So, when these results are considered altogether, it is more logical to conclude that the new addition of the WBS is actually important. Therefore, both of the WBS and WFAF can be recommended to be included in single cell based drying models. Further, we studied the sensitivity of the cell model to different magnitudes of WFAF, WBS, cell wall stiffness and particle resolution which are presented next.

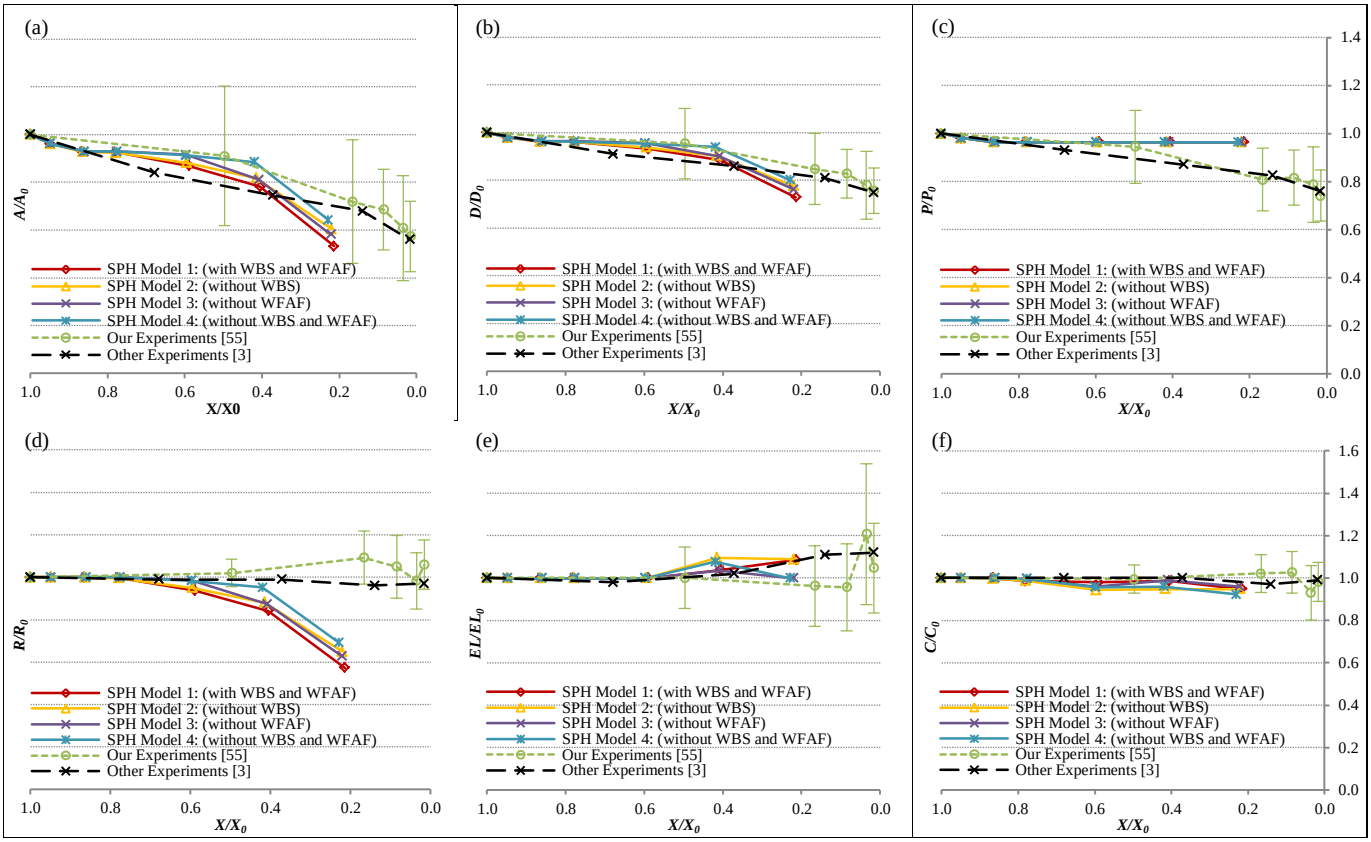

Fig. 9. Effect of cell wall bending stiffness (WBS) and cell wall-fluid attraction forces (WFAF) on normalized cellular parameters: $(a)\ A/A_0$, $(b)\ D/D_0$, $(c)\ P/P_0$, $(d)\ R/R_0$, $(e)\ EL/EL_0$, $(f)\ C/C_0$. (Error bars indicate one standard deviation)

5.4. Model sensitivity to LJ contact strength of WFAF

As presented in Section 5.3, the importance of the WFAF was highlighted and this study was done to further observe the model behaviour at different LJ contact strength of WFAF. To compare the results, the original model (model 1 in Fig. 9) is used as a reference in Fig. 10(c), which has a LJ contact strength of 2×10^{-12} $\mathrm{Nm}^{-1}(= f_0^a)$. As seen from Fig. 10(a), when fairly lower contact strength is used, it is clearly seen that cell fluid unrealistically looses the contact with the cell wall in several locations near the wall boundary. But, when the contact strength is quite high, such separations are not observed as seen from Fig. 10(b) and Fig. 10(c). But, in case if higher contract strengths are used, it causes much local cell wall collapse and self-folding as seen from Fig. 10(d) and Fig. 10(e). Eventually when the contract strength is very high, it leads to produce unrealistic cell shapes as seen from Fig. 10(e). Next, the usual normalized geometric parameters were used to compare the model outcomes for different contact strengths of WFAF and the results are presented in Fig. 11. It is clearly observed from Fig. 11(a), that the higher contact strength values tend to produce significant cell area reductions due to the excessive cellular contractions. A similar trend is observed in case of cell ferret diameter as seen from Fig. 11(b). However, the influence on the cell perimeter seems to be negligible as observed from Fig. 11(c). This may be due to the nature of the wall-fluid attraction forces where they only act if the cell fluid particles tend to separate from the wall boundary. So, they basically make the cell wall move inwards or outwards rather than contracting the cell wall itself to cause perimeter reductions. Next, as seen from Fig. 11(d) when the contact strength is higher, the cell roundness tends to deviate significantly from the experimental curves. In case of cell elongation and compactness, both of the parameters indicate considerable local deviations in case of higher contact strength values (Fig. 11(e) and Fig. 11(f)). These qualitatively and quantitative findings imply that the selection of the appropriate LJ contact strength of cell FWAF should be made with care to avoid significant deviations compared to the experimental findings.

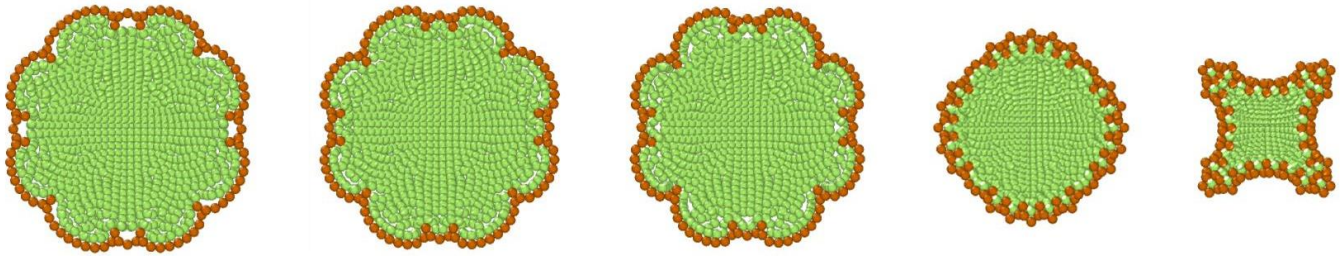

(a) (b) (c) (d) (e)

Fig. 10. Snap shots of dried cells of different LJ contact strengths of WFAF (f_0^a) simulated at X/X_0= 0.2: (*a*) 0.01 f_0^a, (*b*) 0.1 f_0^a, (*c*) f_0^a (= 2 ×10^{-12} Nm^{-1}), (*d*) 5 f_0^a, (*e*) 10 f_0^a.

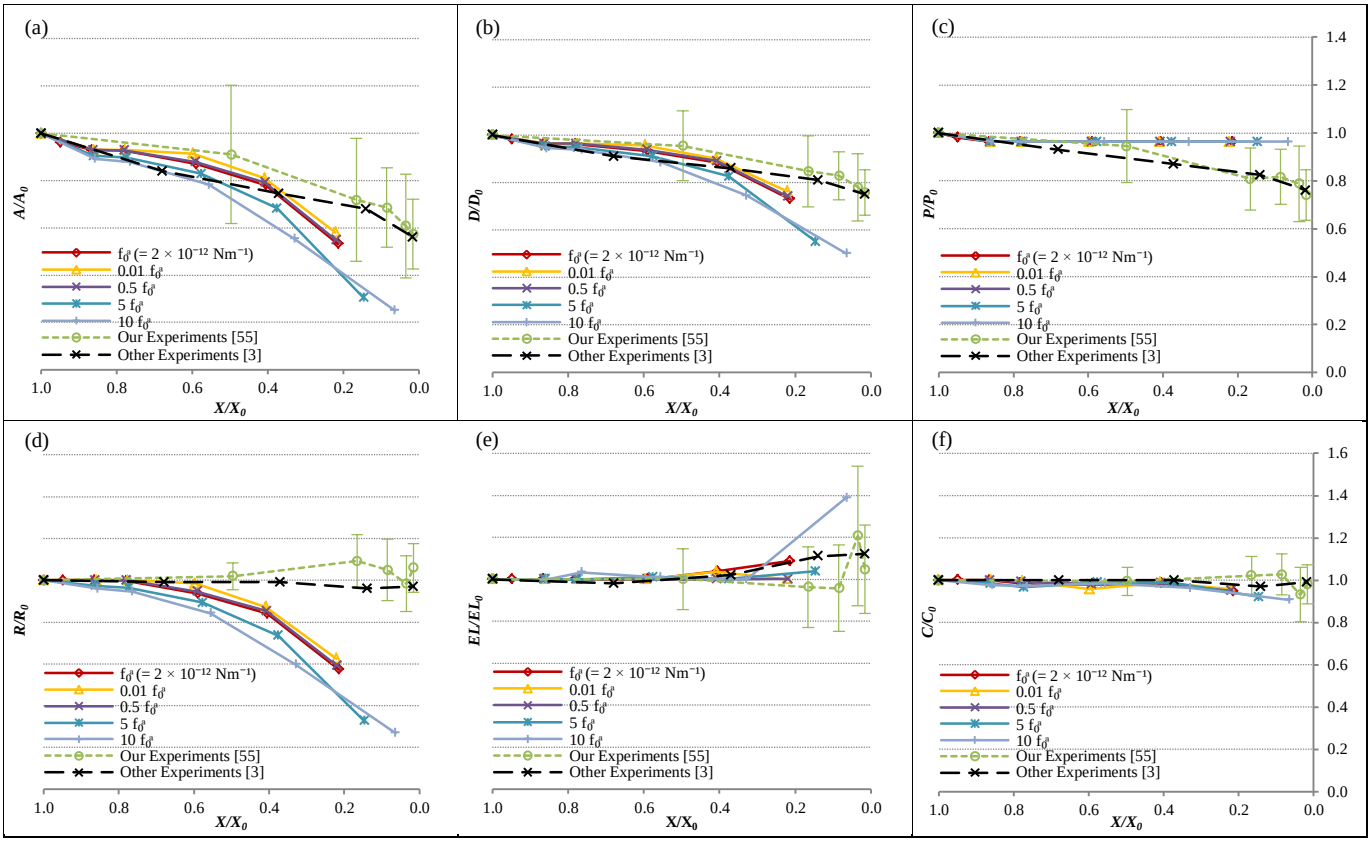

Fig. 11. Effect of LJ contact strength of WFAF (f_0^a) on normalized cellular parameters: (*a*) A/A_0, (*b*) D/D_0, (*c*) P/P_0, (*d*) R/R_0, (*e*) EL/EL_0, (*f*) C/C_0.

5.5. Model sensitivity to cell WBS

In this study, four different cell WBS values were used for the model to study its response and the outcomes are presented in Fig. 12. It is observed that both of the cell shape and the cell area are highly influenced by the cell WBS. Compared to the original model (Fig. 12(c)) which uses 1.0×10^{-11} Nm rad^{-1} (= k_b), lower cell WBS causes cell model to have sharp local cell wall bends as seen in Fig. 12(a) and Fig. 12(b). In case of higher cell WBS values as seen in Fig. 12(d) and Fig. 12(e), the cells tend to experience self folding or collapse of the wall which lead to considerable cell area reduction. Next, to elaborate these effects further, the usual normalized cellular geometrical parameters were considered as presented in Fig. 13. From Fig. 13(a), the normalized cell area trends imply that higher cell WBS causes rapid reduction of cell area during drying which can over-predict the experimental results. As seen in Fig. 13(b), a similar trend is observed for the normalized cell diameter as well. When referring to Fig. 13(c), it is interesting to observe that the cell WBS has hardly any influence on the normalized cell perimeter. This should be due to the nature of the WBS force fields used in the model were, these forces always act normal to wall elements and thereby do not apply any force components along the wall elements to stretch or compress them. Next, as

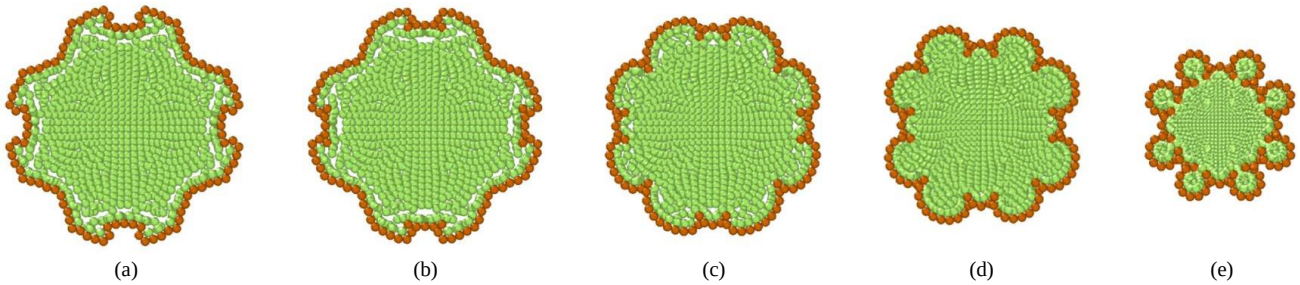

(a) (b) (c) (d) (e)

Fig. 12. Snap shots of dried cells of different cell wall bending stiffness (k_b) simulated at X/X_0= 0.2: (*a*) 0.01 k_b, (*b*) 0.1 k_b, (*c*) k_b (=1.0 × 10^{-11} Nm rad^{-1}), (*d*) 10 k_b, (*e*) 100 k_b.

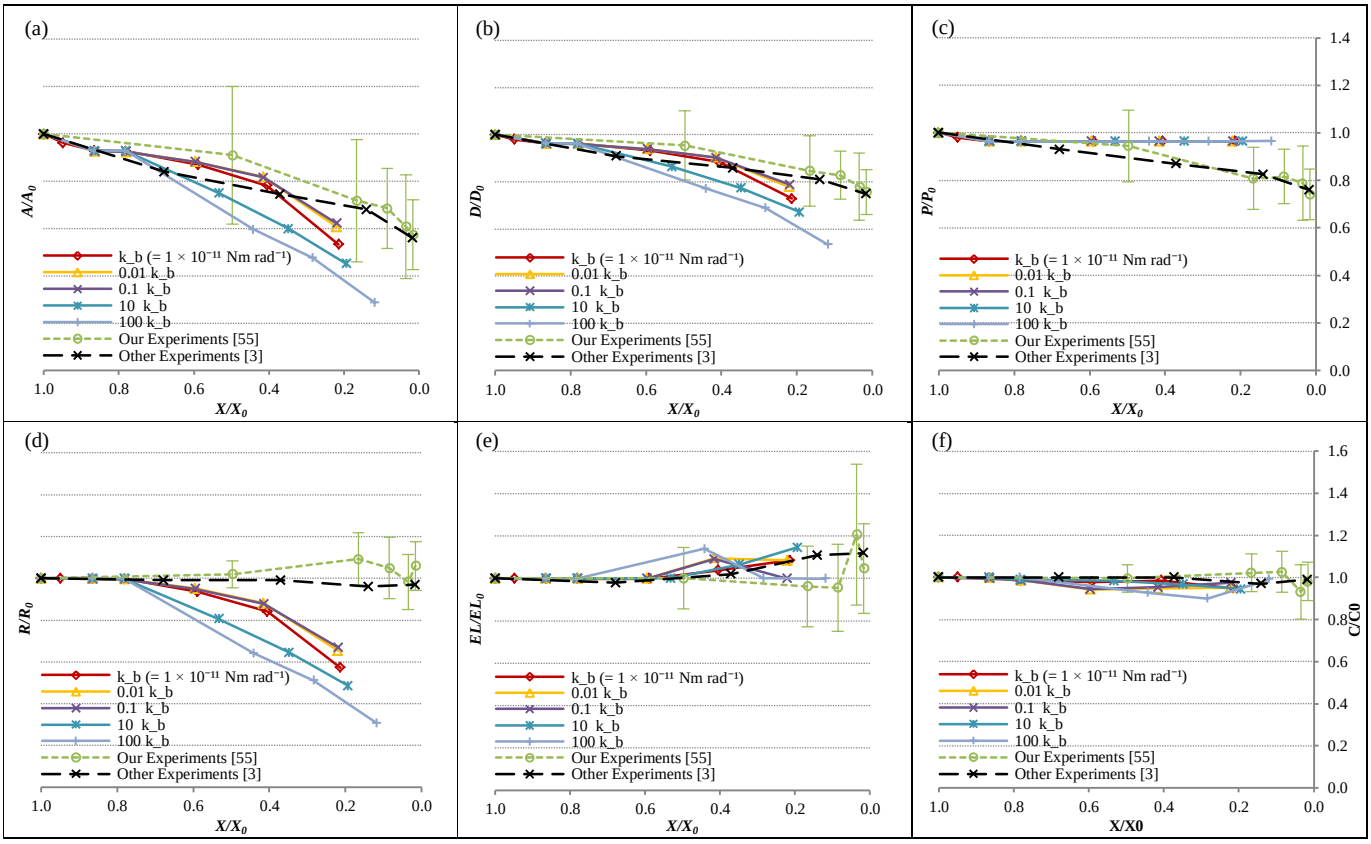

Fig. 13. Effect of cell wall bending stiffness (k_b) on normalized cellular parameters: (*a*) A/A_0, (*b*) D/D_0, (*c*) P/P_0, (*d*) R/R_0, (*e*) EL/EL_0, (*f*) C/C_0.

seen from Fig. 13(d), the cell roundness significantly reduces in case of higher cell WBS values. Further, when referring to Fig. 13(e) and Fig. 13(f), cell elongation and compactness are also influenced by the cell WBS and at the moderately or extremely dried conditions, model predictions tend to significantly deviate from the experimental curves.

5.6. Model sensitivity to cell wall stiffness

Cell wall stiffness is also an important parameter that can influence cellular deformations during drying since it mainly governs the cell wall behaviour both in compression and tension. Wall stiffness can vary based on the characteristics of the fibrous structure of the cell wall, which mainly depends on the product variety and maturity level. To study the model sensitivity to cell wall stiffness, different cell wall stiffness values were used for the model by proportionally varying the $G(\approx E/3)$. For comparison purposes, the original model which uses cell wall stiffness of 54 MPa (= E) is presented in Fig. 14(a). From Fig.

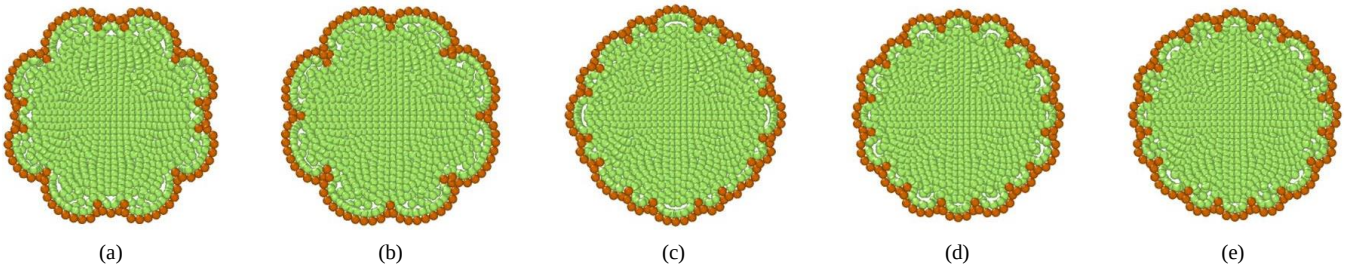

(a) (b) (c) (d) (e)

Fig. 14. Snap shots of dried cells of different cell wall stiffness (E) simulated at X/X_0= 0.2: (a) E (= 54 MPa), (b) $2E$, (c) $4E$, (d) $6E$, (e) $8E$.

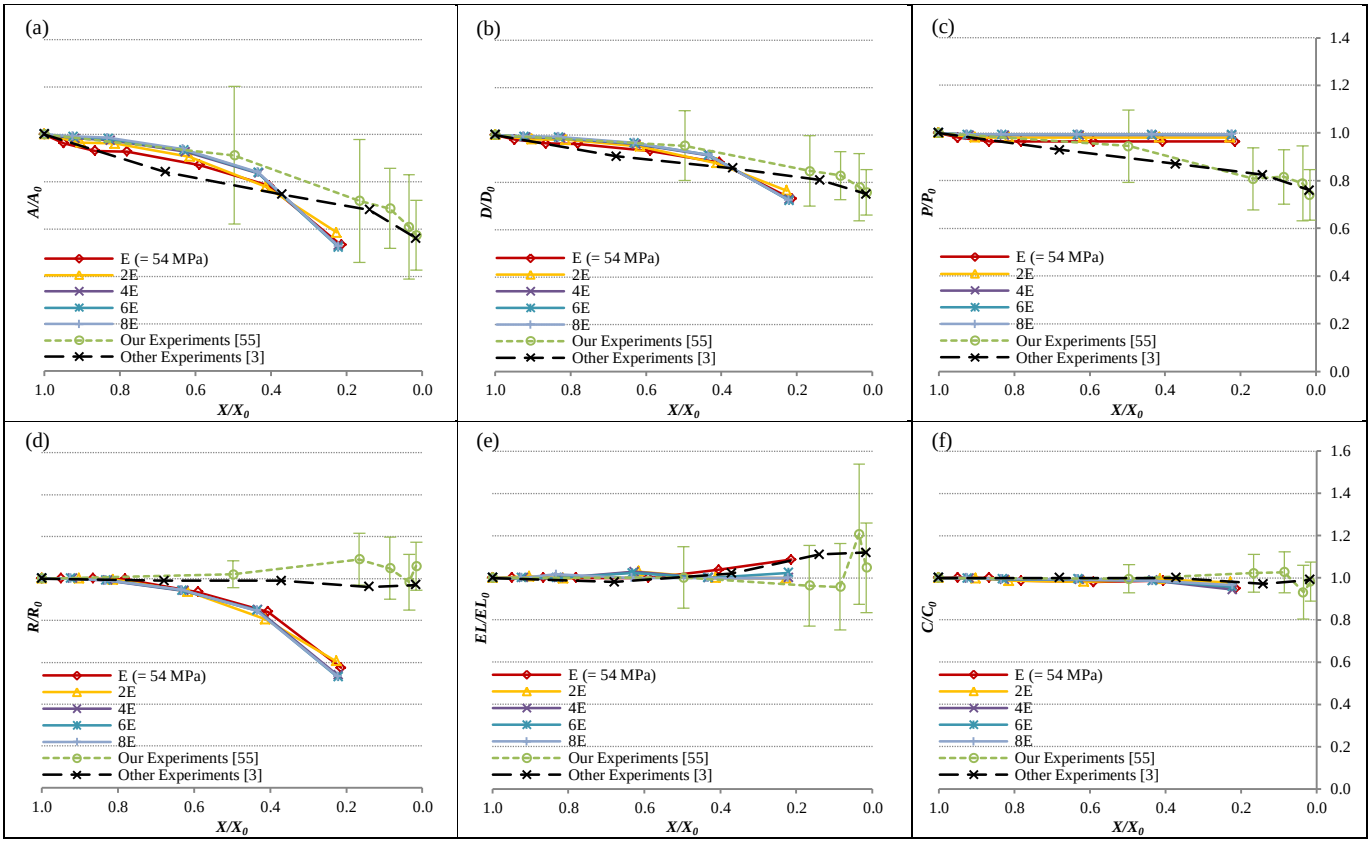

Fig. 15. Effect of cell wall stiffness (E) on normalized cellular parameters: (a) A/A_0, (b) D/D_0, (c) P/P_0, (d) R/R_0, (e) EL/EL_0, (f) C/C_0.

14(b)-(e), the cell visualizations imply that higher cell wall elasticity cause extremely dried cells to have more local wrinkling while restricting the cell wall to undergo uneven collapsing towards the cell centre. Further, as seen in Fig. 15(a), cells that have stiffer cell walls seem to resist the cell area reduction during the initial and intermediate stages of drying. However at the extremely dried conditions, the influence of cell wall stiffness seems not so significant. A similar trend is observed in D/D_0 as seen from Fig. 15(b). From Fig. 15(c), the cell stiffness shows a clear trend of resisting the cell perimeter reductions which can be explained with reference to the spring network used to model the cell wall. Here, the stiffer springs tend to shrink less for a given cell turgor pressure reduction within the initial stages of drying. In case of the cell roundness, as seen from Fig. 15(d), a noticeable influence of cell wall stiffness is only observed in case of extremely dried stages. Both the elongation and compactness seem not much influenced by the cell wall stiffness (Fig. 15(e) and Fig. 15(f)).

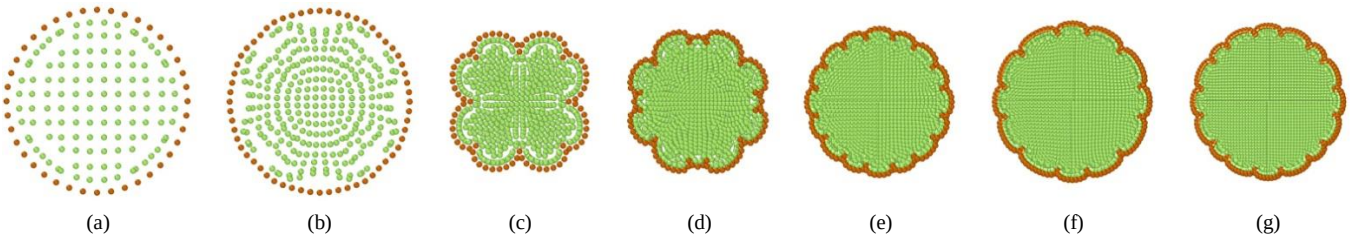

(a) (b) (c) (d) (e) (f) (g)

Fig. 16. Snap shots of dried cell simulations at X/X_0= 0.2 with different particle resolutions: (*a*) n_w= 40; n_f= 120, (*b*) n_w= 60; n_f= 276, (*c*) n_w= 80; n_f= 492, (*d*) n_w= 100; n_f= 788, (*e*) n_w= 120; n_f= 1124, (*f*) n_w= 140; n_f= 1528, (*g*) n_w= 160; n_f= 1992.

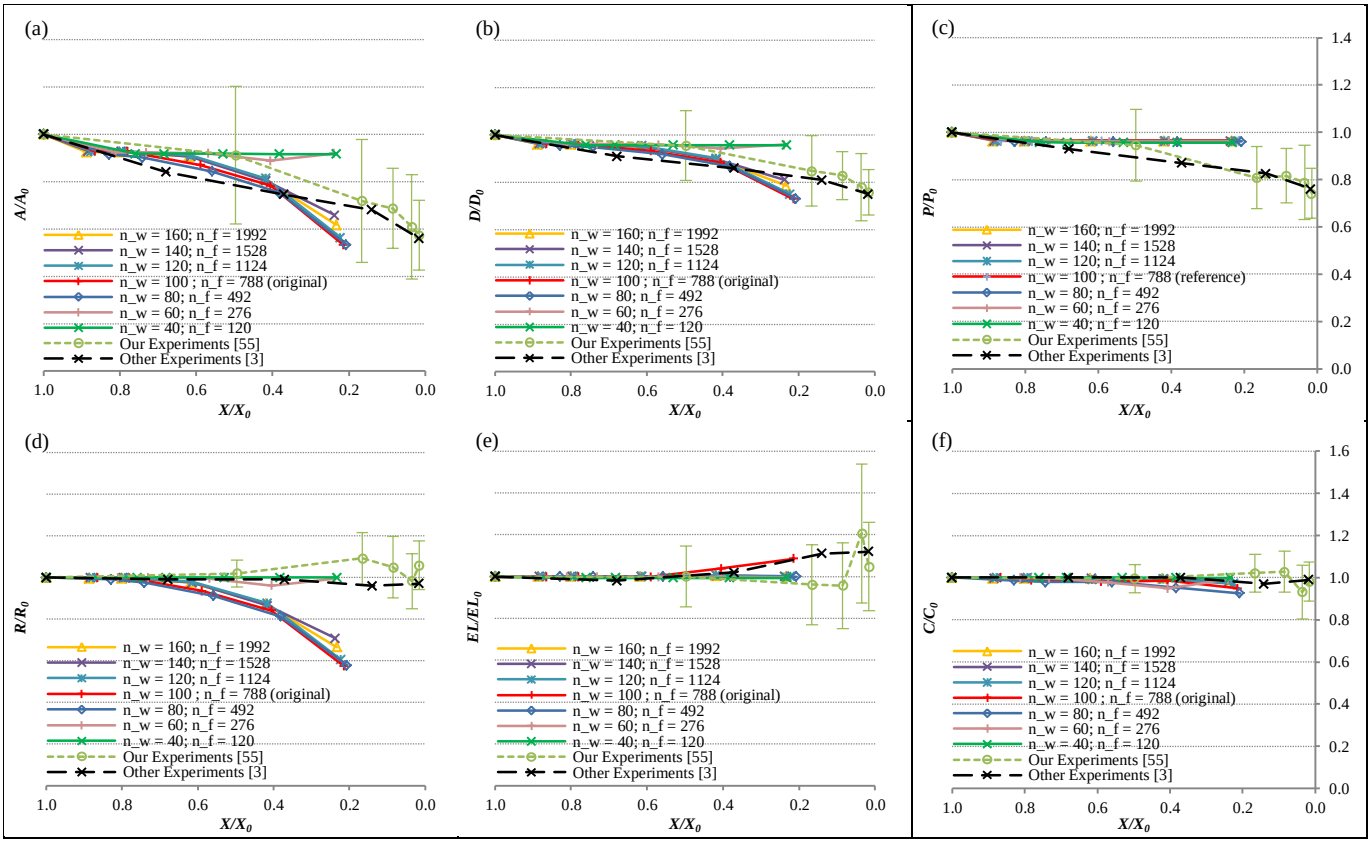

Fig. 17. Effect of cell model particle resolution on normalized cellular parameter predictions: (*a*) A/A_0, (*b*) D/D_0, (*c*) P/P_0, (*d*) R/R_0, (*e*) EL/EL_0, (*f*) C/C_0.

5.7. Model sensitivity to particle resolution

As mentioned in Section 5.1, we observed that the model consistency error varies with the particle resolution. Therefore we used a moderately higher particle resolution (n_w= 100; n_f= 788) for all the above simulations in order to have minimum error bounds at moderate computational costs. Since the particle resolution causes variations in model consistency error, it can result in model prediction variations. So, this study was conducted to investigate particle resolution effects mainly on the cell shape and the geometric parameters. Here also, for comparison purposes the original cell model with n_w= 100 and n_f= 788 is used as a reference which is presented in Fig. 16(d). When comparing the model outcomes, it is observed that the particle resolution has some influence on shapes of extremely dried cells. Specially lower resolution models (Fig. 16(a)-(c)) seems not much experiencing the cell wall wrinkling effects compared to the higher resolution models (Fig. 16(e)-(g)). There is a considerable difference between the cell areas as well. These differences are mainly due to differences of steady state particle settlements which result from different model inconsistencies as discussed in Section 5.1. To elaborate these effects in more detail, the usual cellular parameters were studied and results are presented in Fig. 17. When cell area trends are considered as shown in

Fig. 17(a), the lower resolution models seems not much responding to moisture reduction related cellular shrinkage. In case of higher resolution models, the trends are quite similar to the original model. Similar trends are observed for cell diameter variation as well (Fig. 17(b)). In case of cell perimeter, the particle resolution seems to have almost identical behaviour as can be seen from Fig. 18(c). When considering the cell roundness as seen from Fig. 17(d), the lower resolution models tends to maintain the usual roundness values while higher resolution models tend to experience rapid reduction of roundness with the moisture removal. Compared to the original model, the higher resolution models seem to have slightly lower variations. In case of cell elongation, except the original model, all other models seem to result in fairly fixed elongation (Fig. 17(e)). As seen from Fig. 17(f), all the models seem to have quite lower changes of compactness.

6. Conclusion

A meshfree particle-based model has been developed for micro-scale deformations of plant cells during drying which ensures stable results even at extreme cell deformations. The 2-D single cell model which is presented in this work, is composed of two basic components: a cell fluid model (with SPH) and a cell wall model (with DEM). Simulations for cell deformations have been conducted for a wide range of cellular moisture contents and a reasonable qualitative and quantitative agreement was observed in most of the instances when comparing with the experimental results.

Specifically, we have found that:

- The 2-D single plant cell model can be used to satisfactorily mimic the actual cellular deformations observed in real tissues. However, in some instances, cell geometrical parameters such as cell perimeter and roundness deviated significantly from experimental curves. These imply that the single cell model needs to be further improved with some additional force interactions to accommodate cell wall contractions. Also one possibility for such trends might be the influence of the tissue related intercellular interactions. This potentially interesting effect needs to be further studied using tissue level models.
- Particle resolution significantly influences the model performance in terms of the model consistency error and the computational cost. It leads to cell shape alteration especially in extremely dried states. The model consistency error can be further reduced by maintaining comparable initial gaps between outer most fluid particles and the wall boundary ($\varepsilon_0 / x_0 \leq 0.2$). Also, if around 19 particles are maintained in the influence domain of each fluid particle, the model consistency error was further reduced. By this means, for fresh cell conditions at modest resolutions, we were able to limit the percentage error of model consistency down to 0.07% which is a significant achievement compared to the available SPH-based plant cell models that usually possess about 4% - 7% errors.
- Weakly compressibility was ensured in the cell fluid model since the density fluctuations could be limited to 0.0005%.
- The SPH-DEM coupling is very robust in replicating moisture content and turgor pressure driven cell deformations during drying. It can simulate extreme cellular deformations within a wide range of cell dryness by maintaining good interactions between the cell fluid and the cell wall.
- A moisture domain-based approach can be used to simulate dried cells with an extreme computational advantage.
- Based on the moisture content and the turgor pressure, two distinct stages of cellular deformations were hypothesized and two different approaches were used to simulate the corresponding states of cell dryness. The cell deformations were such that, throughout the first stage, cell turgor pressure remains positive and with the cell moisture content reduction, the cell maintains higher roundness but the perimeter tends to reduce slightly. In the second stage, cell turgor pressure remains almost equal to the atmospheric pressure and cell experiences larger deformations without any sensible cell perimeter reductions and the cell roundness reduces significantly. However, when comparing with the experimental results, deviations were identified in the model predictions which highlight the importance of further numerical and experimental investigations on cell turgor pressure behaviour of cells during drying.
- Fluid transfer through the semi-permeable cell wall is critical for maintaining a fairly good force balance between the cell fluid and the wall in order to relate cell turgor pressure and the cell deformations during drying. Such moisture transfers were accounted in this model and the osmotic potential was used to control the turgor pressure.
- Due to the dimensional shrinkage observed in the cell model during drying, in order to maintain the same number of particles within the influence domain, the smoothing length was adopted using a simple geometrical relationship based on the change of the cell ferret diameter.
- The quartic smoothing kernel was used for the SPH computations in the fluid model other than the commonly used cubic spline kernel which produced unstable solutions in our simulations.
- The state of the art SPH-DEM based plant cell models are found to be not quite suitable for modelling dried cells, since they basically do not involve cell wall-fluid attraction forces and wall bending stiffness effects. The addition of bending stiffness is very critical in avoiding sharp local bends of the cell wall at extremely dried conditions. Also, the

effect of wall-fluid attraction forces was very significant in minimizing unrealistic wall-fluid separations inside the cell such that the wall is sufficiently attached to the contracting cell fluid volume during drying. With both these modifications, the model predictions were quite comparable with the actual dried cell geometry observed in experiments.

- The WFAF, WBS, cell wall stiffness and particle resolution were found to be causing shape changes of the cell model and therefore a good combination of parameters are needed to mimic actual drying behaviour of plant cells.

To conclude, we argue that the proposed novel particle-based cell model provides a reliable means of studying the complex cellular drying phenomena that account even for sub-cellular details. The technique could be further developed with improved cell wall models, adjustments to model parameters, better wall-fluid interaction models and by extending the model up to multi-cell based tissue models incorporating multiscale physics. These can be accommodated within the proposed SPH-DEM particle scheme due to the fundamental adaptability of the meshfree method used. Although we have just focused on apple cells in this work, the method could be applied for other plant cells varieties, provided that the required physical properties and inherited structural characteristics are adequately known.

7. Nomenclature

A	Cell top surface area (m^2)
A_0	Cell top surface area at fresh condition (m^2)
A/A_0	Normalized cell area
A_c	Total surface area of the cylindrical cell (m^2)
C	Cell compactness
C_0	Cell compactness at fresh condition
C/C_0	Normalized cell compactness
D	Cell ferret diameter (m)
D_0	Cell initial diameter at fresh condition (m)
D/D_0	Normalized cell ferret diameter
E	Young's modulus of the cell wall material (MPa)
EL	Cell elongation
EL_0	Cell elongation at fresh condition
EL/EL_0	Normalized cell elongation
F^e	Cell wall stiff forces (N)
F^d	Cell wall damping forces (N)
F^{rf}	Wall-fluid repulsion forces (N)
F^{rw}	Wall-wall repulsion forces (N)
F^a	Wall-fluid attraction forces (N)
F^b	Forces due to bending stiffness of the wall (N)
F^p	Cell fluid pressure forces (N)
F^v	Cell fluid viscous forces (N)
G	Shear modulus of the cell wall material (MPa)
K	Cell fluid compression modulus (MPa)
L	Length of any given discrete wall element (m)
L_0	Initial length of any given discrete wall element (m)
L_p	Cell wall permeability ($m^2N^{-1}s$)
P	Cell perimeter (m)
P_0	Cell perimeter at fresh condition (m)
P/P_0	Normalized cell perimeter
P_a	Pressure of any particle a (Pa)
P_T	Initial cell turgor pressure (Pa)
R	Cell roundness
R_0	Cell roundness at fresh condition
R/R_0	Normalized cell perimeter
S	Ratio between particle distance and smoothing length (r_{ab}/h)
T_0	Initial cell wall thickness (m)
T	Cell wall thickness (m)
W	Smoothing kernel
X	X - coordinate axis

X	Dry basis moisture content at any dried condition (kg $_{water}$/kg $_{dry\ solid}$)
X_0	Dry basis moisture content at fresh condition
X/X_0	Dry basis normalized moisture content
Y	Y - coordinate axis
Z	Cell height (m)
Z	Z - coordinate axis
Z_0	Initial cell height (m)
Z_t	Cell height at the previous time step (m)
$Z_{t+\Delta t}$	Cell height at the current time step (m)
f_0^{rf}	Strength of the LJ repulsion forces between fluid and wall particles ($\mathrm{Nm^{-1}}$)
f_0^{rw}	Strength of the LJ repulsion forces between non-bonded wall particles ($\mathrm{Nm^{-1}}$)
f_0^{a}	Strength of the LJ attraction forces between fluid and wall particles ($\mathrm{Nm^{-1}}$)
h	Smoothing length (m)
h_0	Initial smoothing length (m)
k_b	Bending stiffness of cell wall ($\mathrm{Nm\ rad^{-1}}$)
m_a	Mass of any particle *a* (kg)
n_f	Cell fluid particle number
n_w	Cell wall particle number
r	Cell radius (m)
r_{ab}	Distance between any given particle *a* and *b* (m)
t	Time (s)
v_{ab}	Velocity of any given particle *a* relative to any other particle *b* ($\mathrm{ms^{-1}}$)
x_{ab}	Position vector of any given particle *a* relative to any other particle *b* (m)
Δt	Time step (s)
x_0	Initial fluid grid spacing (m)
$\Delta\theta$	Change of external angle θ of any given wall element (rad)
Π	Osmotic potential of the cell fluid (Pa)
α	Factor governing the relationship between any cell wall element's Z direction extension ratio and λ_θ
β	Parameter that relate 2-D cellular deformations to 3-D cellular deformations
γ	Cell wall damping constant ($\mathrm{Nm^{-1}s}$)
ε_0	Initial minimum allowed gap between any outer most fluid particles and the cell wall (m)
θ	External angle between any adjacent cell wall discrete elements (rad)
λ_θ	Extension ratio of any given cell wall discrete element
μ_a	Dynamic viscosity of any particle *a* (Pa s)
ρ_a	Density of any given particle *a* ($\mathrm{kgm^{-3}}$)
ρ_0	Initial density of the cell fluid ($\mathrm{kgm^{-3}}$)
ρ_a^*	2-D density of any given particle *a* ($\rho_a^* = Z\rho_a$) ($\mathrm{kgm^{-2}}$)

8. Acknowledgements

This research was conducted at the experimental facilities of the Queensland University of Technology (QUT) - Brisbane, Australia and the authors extend their thanks to the graduate student Ms. Parva Hesami for the contributions in experiments. The research studies were financially supported by QUT, International Postgraduate Research Scholarship (IPRS) and Australian Postgraduate Award (APA) scholarship. Support from the ARC Future Fellowship grant (FT100100172) and the high performance computer resources provided by the QUT are also gratefully acknowledged as is the support by University of Ruhuna - Sri Lanka.

9. References

[1] S. Grabowski, M. Marcotte, and H. S. Ramaswamy, "Drying of Fruits, Vegetables, and Spices " in *Handbook of postharvest technology : cereals, fruits, vegetables, tea, and spices*, A. Chakraverty, A. S. Mujumdar, G. S. V. Raghavan, and H. Rawaswamy, Eds., ed New York Marcel Dekker, 2003, pp. 653-695.

[2] S. V. Jangam, "An Overview of Recent Developments and Some R&D Challenges Related to Drying of Foods," *Drying Technol.,* vol. 29, pp. 1343-1357, 2011.

[3] L. Mayor, M. A. Silva, and A. M. Sereno, "Microstructural Changes during Drying of Apple Slices," *Drying Technol.,* vol. 23, pp. 2261-2276, 2005.

[4] J. E. Lozano, E. Rotstein, and M. J. Urbicain, "Total porosity and open-pore porosity in the drying of fruits," *J. Food Sci.,* vol. 45, pp. 1403-1407, 1980.

[5] I. N. Ramos, C. L. M. Silva, A. M. Sereno, and J. M. Aguilera, "Quantification of microstructural changes during first stage air drying of grape tissue," *J. Food Eng.,* vol. 62, pp. 159-164, 2004.

[6] B. P. Hills and B. Remigereau, "NMR studies of changes in subcellular water compartmentation in parenchyma apple tissue during drying and freezing," *Int. J. Food Sci. Tech.,* vol. 32, pp. 51-61, 1997.

[7] C. Y. Lee, D. K. Salunkhe, and F. S. Nury, "Some chemical and histological changes in dehydrated apple," *J. Sci. Food Agric.,* vol. 18, pp. 89-93, 1967.

[8] P. P. D. Lewicki, J., "Effect of drying on tissue structure of selected fruits and vegetables," in *Proceedings of the 11th International Drying Symposium Drying 98*, Greece, 1998, pp. 1093-1099.

[9] P. P. Lewicki and G. Pawlak, "Effect of Drying on Microstructure of Plant Tissue," *Drying Technol.,* vol. 21, pp. 657-683, 2003/01/06 2003.

[10] M. K. Bartlett, C. Scoffoni, and L. Sack, "The determinants of leaf turgor loss point and prediction of drought tolerance of species and biomes: a global meta-analysis," *Ecol. Lett.,* vol. 15, pp. 393-405, 2012.

[11] G. H. Crapiste, S. Whitaker, and E. Rotstein, "Drying of cellular material—I. A mass transfer theory," *Chem. Eng. Sci.,* vol. 43, pp. 2919-2928, 1988-a.

[12] T. Rudge and J. Haseloff, "A Computational Model of Cellular Morphogenesis in Plants," in *Advances in Artificial Life*. vol. 3630, M. Capcarrère, A. Freitas, P. Bentley, C. Johnson, and J. Timmis, Eds., ed: Springer Berlin Heidelberg, 2005, pp. 78-87.

[13] H. Honda, H. Yamanaka, and M. Dan-Sohkawa, "A computer simulation of geometrical configurations during cell division," *J. Theor. Biol.,* vol. 106, pp. 423-435, 1984.

[14] K. Fleischer, Barr, A. H. , "A Simulation Testbed for the Study of Multicellular Development: The Multiple Mechanisms of Morphogenesis.," in *Artificial Life III Redwood*, CA, Addison-Wesley, 1994, pp. 389-416.

[15] H. Honda, M. Tanemura, and T. Nagai, "A three-dimensional vertex dynamics cell model of space-filling polyhedra simulating cell behavior in a cell aggregate," *J. Theor. Biol.,* vol. 226, pp. 439-453, 2004.

[16] H. X. Zhu and J. R. Melrose, "A Mechanics Model for the Compression of Plant and Vegetative Tissues," *J. Theor. Biol.,* vol. 221, pp. 89-101, 2003.

[17] C. X. Wang, L. Wang, and C. R. Thomas, "Modelling the Mechanical Properties of Single Suspension-Cultured Tomato Cells," *Ann. Bot.,* vol. 93, pp. 443-453, 2004.

[18] N. Wu and M. J. Pitts, "Development and validation of a finite element model of an apple fruit cell," *Postharvest Biol. Technol.,* vol. 16, pp. 1-8, 1999.

[19] Q. Gao and R. E. Pitt, "Mechanics of parenchyma tissue based on cell orientation and microstructure," *Transactions of the ASABE,* vol. 34, pp. 0232-0238, 1991.

[20] R. E. Pitt, "Models for the Rheology and Statistical Strength of Uniformly Stressed Vegetative Tissue," *Transactions of the ASABE,* vol. 25, pp. 1776-1784, 1982.

[21] G. R. Liu and M. B. Liu, *Smoothed Particle Hydrodynamics : A Meshfree Particle Method*. Singapore: World Scientific Publishing Co., 2003.

[22] T. Belytschko, Y. Krongauz, D. Organ, M. Fleming, and P. Krysl, "Meshless methods: An overview and recent developments," *CMAME,* vol. 139, pp. 3-47, 1996.

[23] R. A. Gingold and J. J. Monaghan, "Smoothed particle hydrodynamics - Theory and application to non-spherical stars," *MNRAS,* vol. 181, pp. 375-389, 1977.

[24] T. Belytschko, Y. Y. Lu, and L. Gu, "Element-free Galerkin methods," *IJNME,* vol. 37, pp. 229-256, 1994.

[25] G. R. Liu and Y. T. Gu, "A point interpolation method for two-dimensional solids," *IJNME,* vol. 50, pp. 937-951, 2001.

[26] G. R. Liu and Y. T. Gu, "Comparisons of two meshfree local point interpolation methods for structural analyses," *CompM,* vol. 29, pp. 107-121, 2002/08/01 2002.

[27] S. Atluri and T. Zhu, "A new meshless local Petrov-Galerkin (MLPG) approach in computational mechanics," *CompM,* vol. 22, pp. 117-127, 1998.

[28] G. R. Liu and Y. T. Gu, "A local radial point interpolation method (LRPIM) for free vibration analyses of 2-d solids," *J. Sound Vibrat.*, vol. 246, pp. 29-46, 2001.
[29] G. R. Liu and Y. T. Gu, "Boundary meshfree methods based on the boundary point interpolation methods," *Eng. Anal. Bound. Elem.*, vol. 28, pp. 475-487, 2004.
[30] Y. Wu, G. Liu, and Y. Gu, "Application of meshless local Petrov-Galerkin (MLPG) approach to simulation of incompressible flow," *Numer. Heat Transfer, Part B*, vol. 48, pp. 459-475, 2005.
[31] Y. T. Gu, Q. X. Wang, and K. Y. Lam, "A meshless local Kriging method for large deformation analyses," *CMAME*, vol. 196, pp. 1673-1684, 2007.
[32] Y. T. Gu and G. R. Liu, "Meshless techniques for convection dominated problems," *CompM*, vol. 38, pp. 171-182, 2006/07/01 2006.
[33] P. Van Liedekerke, P. Ghysels, E. Tijskens, G. Samaey, D. Roose, and H. Ramon, "Mechanisms of soft cellular tissue bruising. A particle based simulation approach," *Soft Matter*, vol. 7, pp. 3580-3591, 2011.
[34] P. V. Liedekerke, P. Ghysels, E. Tijskens, G. Samaey, B. Smeedts, D. Roose, and H. Ramon, "A particle-based model to simulate the micromechanics of single-plant parenchyma cells and aggregates," *PhBio*, vol. 7, p. 026006, 2010.
[35] P. Van Liedekerke, E. Tijskens, H. Ramon, P. Ghysels, G. Samaey, and D. Roose, "Particle-based model to simulate the micromechanics of biological cells," *PhRvE*, vol. 81, p. 061906, 2010.
[36] H. C. P. Karunasena, W. Senadeera, Y. T. Gu, and R. J. Brown, "A Coupled SPH-DEM Model for Fluid and Solid Mechanics of Apple Parenchyma Cells During Drying," in *18th Australian Fluid Mechanics Conference*, Launceston - Australia, 2012b.
[37] H. C. P. Karunasena, W. Senadeera, Y. T. Gu, and R. J. Brown, "A particle based micromechanics model to simulate drying behaviors of vegetable cells," in *4th International Conference on Computational Methods (ICCM 2012)*, Gold Coast, Australia, 2012a.
[38] L. Taiz and E. Zeiger, *Plant Physiology* 3rd ed. Sunderland-Massachusetts: Sinauer Associates, 2002.
[39] S. B. Nilsson, C. H. Hertz, and S. Falk, "On the Relation between Turgor Pressure and Tissue Rigidity. II," *Physiol. Plant.*, vol. 11, pp. 818-837, 1958.
[40] A. E. Smith, K. E. Moxham, and A.P.J, "On uniquely determining cell–wall material properties with the compression experiment," *Chem. Eng. Sci.*, vol. 53, pp. 3913-3922, 1998.
[41] H.-I. Wu, R. D. Spence, P. J. H. Sharpe, and J. D. Goeschl, "Cell wall elasticity: I. A critique of the bulk elastic modulus approach and an analysis using polymer elastic principles," *Plant, Cell Environ.*, vol. 8, pp. 563-570, 1985.
[42] M. C. Jarvis, "Intercellular separation forces generated by intracellular pressure," *Plant, Cell Environ.*, vol. 21, pp. 1307-1310, 1998.
[43] M. A. J. Chaplain, "The Strain Energy Function of an Ideal Plant Cell Wall," *J. Theor. Biol.*, vol. 163, pp. 77-97, 1993.
[44] D. R. P. Hettiaratchi and J. R. O'Callaghan, "Structural mechanics of plant cells," *J. Theor. Biol.*, vol. 74, pp. 235-257, 1978.
[45] D. G. Hepworth and D. M. Bruce, "Measuring the Deformation of Cells within a Piece of Compressed Potato Tuber Tissue," *Ann. Bot.*, vol. 86, pp. 287-292, August 1, 2000 2000.
[46] S. M. Hosseini and J. J. Feng, "A particle-based model for the transport of erythrocytes in capillaries," *Chem. Eng. Sci.*, vol. 64, pp. 4488-4497, 2009.
[47] T. W. Pan and T. Wang, "Dynamical simulation of red blood cell rheology in microvessels," *Int. J. Numer. Anal. Model.*, vol. 6, pp. 455-473, 2009.
[48] L. Shi, T.-W. Pan, and R. Glowinski, "Deformation of a single red blood cell in bounded Poiseuille flows," *PhRvE*, vol. 85, p. 016307, 2012.
[49] P. V. Liedekerke, P. Ghysels, E. Tijskens, G. Samaey, B. Smeedts, D. Roose, and H. Ramon, "A particle based model to simulate plant cells dynamics," presented at the 4th international SPHERIC workshop, Nantes, France, 2009.
[50] J. P. Morris, P. J. Fox, and Y. Zhu, "Modeling Low Reynolds Number Incompressible Flows Using SPH," *JCoPh*, vol. 136, pp. 214-226, 1997.
[51] G. R. Liu and M. B. Liu. (2003). *Smoothed Particle Hydrodynamics : A Meshfree Particle Method*.
[52] L. Taiz and E. Zeiger, "Water and Plant Cells," in *Plant Physiol.*, ed: Sinauer Associates, 2010, pp. 73-84.
[53] A. Stukowski, "Visualization and analysis of atomistic simulation data with OVITO–the Open Visualization Tool," *Modell. Simul. Mater. Sci. Eng.*, vol. 18, p. 015012, 2010.
[54] C. V. Willigen, J. M. Farrant, and N. W. Pammenter, "Anomalous Pressure Volume Curves of Resurrection Plants Do Not Suggest Negative Turgor," *Ann. Bot.*, vol. 88, pp. 537-543, October 1, 2001 2001.
[55] H. C. P. Karunasena, P. Hesami, W. Senadeera, Y. T. Gu, R. J. Brown, and A. Oloyede, "Scanning Electron Microscopic Study of Apple during Drying," *Drying Technol.*, in press.
[56] J. C. Araujo, F. C. Téran, R. A. Oliveira, E. A. A. Nour, M. A. P. Montenegro, J. R. Campos, and R. F. Vazoller, "Comparison of hexamethyldisilazane and critical point drying treatments for SEM analysis of anaerobic biofilms and granular sludge," *J. Electron Microsc.*, vol. 52, pp. 429-433, September 24, 2003 2003.

[57] D. F. Bray, J. Bagu, and P. Koegler, "Comparison of hexamethyldisilazane (HMDS), Peldri II, and critical-point drying methods for scanning electron microscopy of biological specimens," *Microsc. Res. Tech.*, vol. 26, pp. 489-495, 1993.
[58] P. W. Cleary and J. J. Monaghan, "Conduction Modelling Using Smoothed Particle Hydrodynamics," *JCoPh*, vol. 148, pp. 227-264, 1999.
[59] J. J. Monaghan, "Smoothed particle hydrodynamics," *Rep. Prog. Phys.*, vol. 68, p. 1703, 2005.
[60] N. J. Quinlan, M. Basa, and M. Lastiwka, "Truncation error in mesh-free particle methods," *IJNME*, vol. 66, pp. 2064-2085, 2006.